Doctoral Dissertations and Master's Theses

Winter 12-8-2022

Multifrequency Scintillation in the Polar Caps

Tate Colby
Embry-Riddle Aeronautical University, colbyt@my.erau.edu

MULTIFREQUENCY SCINTILLATION IN THE POLAR CAPS

BY
TATE COLBY

A Thesis

Submitted to the Department of Physical Sciences

In partial fulfillment of the requirements

for the degree of

Master of Science in Engineering Physics

11/2022

Embry-Riddle Aeronautical University

Daytona Beach, Florida

MULTIFREQUENCY SCINTILLATION IN THE POLAR CAPS

by

Tate Colby

This thesis was prepared under the direction of the candidate's Thesis Committee Chair, Dr. Matthew D Zettergren, PhD, Assistant Professor, Daytona Beach Campus, and Dissertation Committee Members Dr. Kshitija Deshpande, PhD, Associate Professor, Daytona Beach Campus, and Dr. Leslie J Lamarche, PhD, Research Engineer, SRI International, and has been approved by the Thesis Committee. It was submitted to the Department of Physical Sciences in partial fulfillment of the requirements of the degree of
Master of Science in Engineering Physics

THESIS COMMITTEE:

Matthew Zettergren
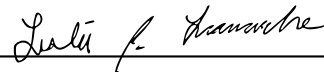
Dr. Matthew D Zettergren, PhD,
Committee Chair

Dr. Kshitija Deshpande, PhD,
Committee Member

Dr. Leslie J Lamarche, PhD,
Committee Member

Dr. Edwin Mierkiewicz, PhD,
Graduated Program Chair,
Engineering Physics

Dr. John Hughes, PhD,
Department Chair,
Physical Sciences

Dr. Peter Hoffmann, PhD,
Dean, College of Arts and Sciences

Dr. Christopher Grant, PhD,
Vice Provost of Academic Support

Abstract

In the ionosphere, plasma density structures with scales sizes ranging from a few centimeters to hundreds of kilometers are capable of modifying the phase and amplitude of a radio signal in a rapid random manner in a process called scintillation. The Coherent Electromagnetic Radio Tomography (CERTO) and the Canadian High Arctic Ionospheric Network (CHAIN) are two different networks of scintillation receivers, each with a station in Resolute Bay, Canada. CERTO measures amplitude and phase signals in VHF and UHF while CHAIN measures amplitude and phase signals in the L-band. Through these measurements we can calculate the scintillation indexes, S_4 and σ_ϕ to gain insight into the plasma density structures the scintillation originated from.

In this Thesis, the processes of detrending and processing VHF σ_ϕ from CERTO data and L-band S_4 & σ_ϕ CHAIN data are detailed and the resulting scintillation data are analyzed by comparing the time of events to data from the Resolute Bay Incoherent Scatter Radar (RISR), creating histograms of the total scintillation data acquired, and by examining CERTO σ_ϕ data results with respect to elevation angle.

This work concludes that detrending scintillation data at frequencies other than L-band is not a trivial process and must be given care in order to produce accurate results. Within this work none of the RISR data contained significant plasma density during any of the satellite conjunctions analyzed. The histograms of total VHF and L-band σ_ϕ values show more variation in the average VHF σ_ϕ values than in the L-band σ_ϕ. A positive correlation between the satellites elevation angle and increase in σ_ϕ is identified.

Acknowledgments

Contents

List of Tables

List of Figures

Chapter 1

INTRODUCTION

1.1 The Ionosphere

The Earth's ionosphere is a region of the upper atmosphere that extends 50-1,000 km in altitude that contains a high concentration of free electrons and ions mixed with neutral particles. Electron density will peak in accordance to two competing occurrences. As solar illumination and particle precipitation ionize the neutral particles the density of ions increases at lower altitudes compared to higher altitudes because there are more neutral molecules present at lower altitudes. However, below a certain altitude ionizing radiation does not penetrate the atmosphere easily, reducing the ion density. This altitude is where the density peak occurs and this altitude varies with time of day, location, season, and solar cycle [Lamarche, 2017]. Since the ionosphere contains many different ion species it is helpful to discuss the plasma density in terms of electron density. A model representation of electron density changes with altitude for day and night times are shown in Figure 1.1.

Within varying altitudes of the ionosphere are three regions. The D-region extends from ~80 km up to ~90 km and typically only exists when the ionosphere is sunlit. The E-region extends from ~90 km up to ~130 km with a density peak between ~105 and ~100 km, depending of the time of day and season. The altitudes of the ionospheric regions are only estimates for these same reasons. The F-region extends above ~130 km and has a density peak at ~250 km [Kivelson and Russell, 1995]. The
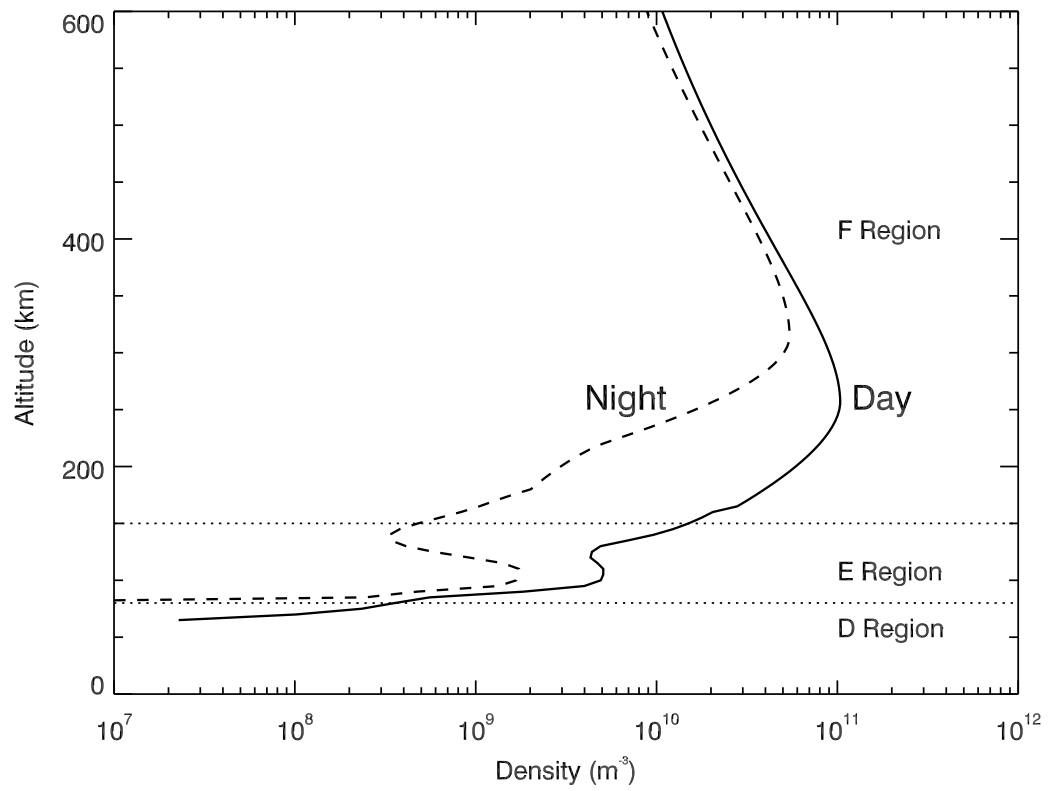
Figure 1.1: Altitude profiles of electron density throughout the ionosphere found from the IRI model. Typical extents of the D, E, and F regions are identified. Taken from [Lamarche, 2017].

F-region may sometimes have two peaks under certain daytime conditions. Notice how in Figure 1.1 the daytime profile in the solid line generally has a higher density at all altitudes compared to the nighttime profile in the dotted line. This is due to the lack of photoionization during the night time. Night time electron densities may be higher during aurora or sporadic E-layer. The density profile is also variable with respect to the seasons and solar cycle in addition to the time of day.

Plasma density waves or structures, also known as irregularities, within the polar cap can occur on scale sizes ranging from thousands of kilometers to less than a centimeter [Tsunoda, 1988]. Plasma irregularities are categorized in three sizes; large-scale, intermediate-scale, and small-scale plasma irregularities. These the scale sizes for these irregularities are greater than 30 km, between 100 m and 30 km, and below 100 m for the large, intermediate, and small-scale plasma irregularities, respectively [Kelley, 2009]. This thesis is concerned with the intermediate-scale plasma irregularities, as these are scintillation causing structures. Intermediate-scale sized structures are created from plasma instabilities such as Gradient Drift Instabilities (GDI) and Kelvin-Helmholtz Instabilities (KHI).
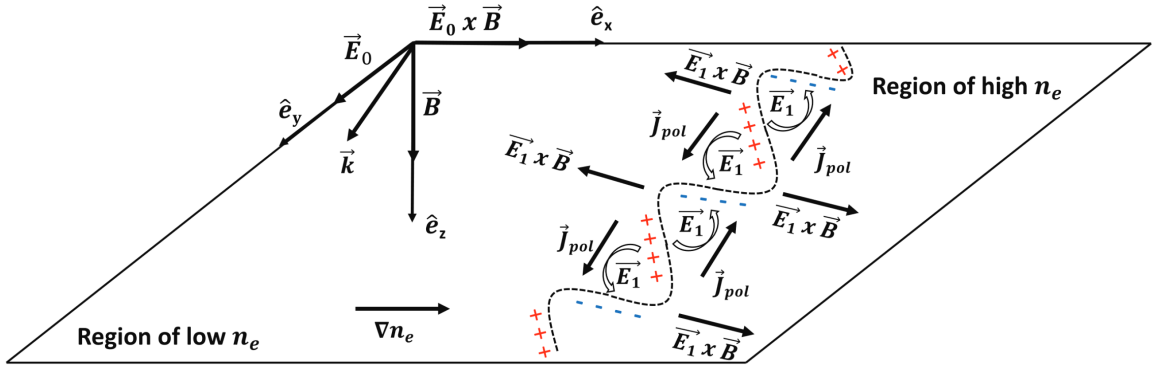
Figure 1.2: Charge accumulation resulting in gradient-drift instability (GDI). Taken from [Deshpande et al., 2021]

GDI are largely associated with the F region ionosphere and occur when density perturbations are applied to a background plasma gradient that is oriented in the same direction of plasma drifts. Figure 1.2 shows an illustration of this process. Within the perturbation charges accumulate on opposite sides, creating other electric
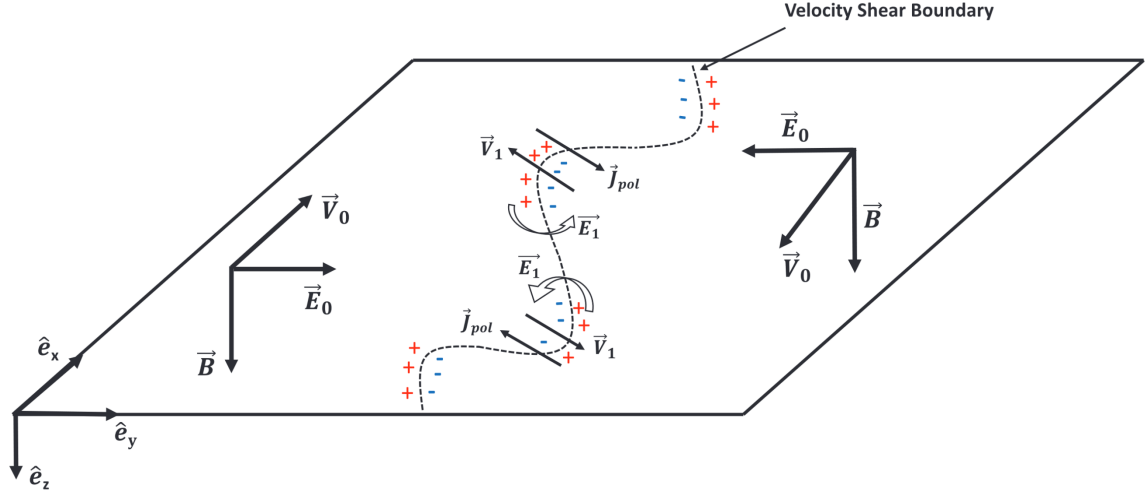
Figure 1.3: Kelvin-Helmholtz instability (KHI) resulting from a flow shear. Taken from [Deshpande et al., 2021]

fields, $\mathbf{E_1}$. These other electric fields, called electric perturbation fields, create $\mathbf{E_1} \times \mathbf{B}$ that reinforce the seed density perturbations, resulting in unstable growth similar in structure to Rayleigh Taylor instabilities. KHI are share instabilities that originate from background plasma velocity shear across a relatively narrow boundary layer. If plasma velocity normal to the shear region is perturbed, it results in a nonuniform polarization current that causes charge accumulation and produces an electric field that stimulates growth of the instability. This is shown in Figure 1.3.

1.2 Scintillation

Intermediate-scale sized plasma structures less than the Fresnel scale ($\sqrt{2\lambda z}$, λ: wavelength of signal, z: altitude above receiver [Forte and Radicella, 2002], [Ghobadi et al., 2020]) modify the phase and amplitude of a radio signal in a rapid random manner by diffraction in a process called scintillation. Diffraction of a signal causes rapid fluctuations of both phase and amplitude while refraction only triggers phase fluctuations. Irregularities of a size greater than the Fresnel scale cause refractive effects while irregularities smaller than Fresnel scale sizes produce both refractive and diffractive effects. The Fresnel scale near peak irregularities in F-region of ionosphere is ~350

km [Yeh and Liu, 1982]. These rapid variations vary with the latitude, season, and geomagnetic conditions and can cause lead to problems of loss-of-lock, accuracy degradation, and other deleterious effects to signal data [Kintner et al., 2007]. These rapid variations can also be used to characterize the fundamental plasma processes related to scintillation [Deshpande et al., 2021].

Qualitatively, amplitude and phase scintillation indices are measured in two different ways with respect to the input amplitude and phase signals. Amplitude scintillation is classically defined as the ratio of standard deviation of the signal power to the mean signal power computed over a period of time as,

$$S_4 = \sqrt{\frac{\langle I^2 \rangle - \langle I \rangle^2}{\langle I \rangle^2}} \qquad (1.1)$$

where I is the received power and $\langle \cdot \rangle$ is a temporal average. Phase scintillation calculated as the standard deviation of the detrended phase data as,

$$\sigma_\phi = \sqrt{\langle \phi^2 \rangle - \langle \phi \rangle^2} \qquad (1.2)$$

where ϕ is the detrended phase. In many studies, scintillation indices are evaluated every minute or recommended to be evaluated every minute [Jin et al., 2014, Pan and Yin, 2014, Wang et al., 2016, Mushini et al., 2012, Jayachandran et al., 2009, Ghobadi et al., 2020]. However, this time period may be arbitrarily larger or smaller, with the main restriction that the time period be long compared to the Fresnel length divided by the irregularity drift speed [Kintner et al., 2007]. The rational for detrending the phase data stems from the desire to include only high-frequency fluctuations due to diffraction in the phase scintillation index. The commonly adopted method of phase detrending is a sixth-order high-pass digital Butterworth filter, which removes all low frequency effects below its nominal frequency cut-off of 0.1 Hz [Van Dierendonck and Arbesser-Rastburg, 2004]. This cut-off frequency implies a relative plasma drift velocity of about 36.5 m/s as [Ghobadi et al., 2020] showcases for an example and herein lies the problem. These values appear suitable for the geometry encountered in low-latitude ionosphere while the values are always too low for the polar caps,

where plasma convection velocity is between 100 and 1000 m/s [Forte and Radicella, 2004]. Utilizing this frequency cut-off at high latitudes can lead to a misleading data interpretation such as an overestimation of the phase scintillation index [Ghobadi et al., 2020],[Forte and Radicella, 2002].

1.3   Incoherent Scatter Radars

Incoherent Scatter Radar (ISR) is a type of radar system that uses scatter generated by ionospheric plasma to deduce parameters of the ionosphere. ISRs are commonly used to resolve plasma density enhancements and have been the subject of the most irregularity studies as a result at how effective they are [Nishimura et al., 2021]. All ISR facilities are structured uniquely, having been developed in different time periods and covering different regions of Earth, ISRs have evolved to adapt to their region of operation. As time passes and technology advances, designs for ISRs improve and the latest generation of radars are the Advanced Modular Incoherent Scatter Radar (AMISR). The AMISR model is designed to be flexible, reliable, remotely operated, and relocatable. AMISR has a phased array consiting of Antenna Element Units (AEU), which are cross-dipole antennas with a 500-Watt solid state power amplifier [Valentic et al., 2013]. The AEUs are grouped into packs of 32 on a flat panel and each AMISR face contains 128 panels for a total of 4096 AEUs that totals to approximately 2MW of peak transmit power.

The AMISR relevant for this thesis are the two Resolute Bay Incoherent Scatter Radars (RISR), RISR-North (RISR-N) and the Canadian Resolute Bay Incoherent Scatter Radar (RISR-C), which cover measurements of polar cap electrodynamics. The radars are located at 74.7° N, 94.9° W geographic which makes them ideal for observations of polar plasma density irregularities. Both AMISRs are located next to each other facing North for RISR-N and South for RISR-C at Resolute Bay. Our goals with RISR is to plot electron density during the same time as our data to see if any of the data land within any density enhancements and observe differences in this data to other data outside of density enhancements. However, one of the main drawbacks of all ISRs is the cost of operation, as such, ISRs data is not always available. This

thesis will work around these limitations in Section 3.1.2.

1.4 CERTO

The Coherent Electromagnetic Radio Tomography (CERTO) is a constellation of ra-
dio beacons that take measurements of ionospheric Total Electron Content (TEC) and
radio scintillations. A number of satellites in Low Earth Orbit (LEO) carry CERTO
beacons. The satellites that have been identified to transmit data to the reciver in Res-
olute Bay are CASSIOPE, COSMOS2407, F15, and COSMOS2414 [Lamarche et al.,
2020]. The CERTO beacon provides continuous wave transmissions from satellites at
VHF (150.012 MHz), UHF (400.032 MHz), and L-band (1066.752 MHz) frequencies
sampled at rate of 50 Hz [Bernhardt and Siefring, 2006]. Ground receivers detect
these signals when a CERTO beacon carrying satellite is over the horizon, which
allows CERTO systems to monitor ionospheric scintillations within the region be-
tween the beacon and ground receiver. The ground receiver can then take measures
of the phase and amplitude fluctuations for the CERTO radio source [Bernhardt and
Siefring, 2006]. According to the design of the CERTO beacons, S_4 can reach up to 1.4
and S_4 below $\sim$0.3 might be considered moderate scintillations [Siefring et al., 2015].
In July 2017, a CERTO receiver was installed at Resolute Bay. This receiver was
operational between July 2017 and January 2018. The Resolute Bay CERTO bea-
con receiver measures the VHF phase against the UHF phase, so UHF phase should
be near zero while VHF phase is the differential phase. This thesis will extensively
analyze the VHF phase data from CERTO.

1.5 CHAIN

The Canadian High Arctic Ionospheric Network (CHAIN) is a distributed array of
radio instruments primarily in the polar cap. CHAIN consist of ten dual frequency
high data Global Positioning System (GPS) receivers and six digital ionosondes. The
GPS satellites that transmit data to CHAIN receivers orbit in Greater Earth Orbit
(GEO). The CHAIN ground receiver can track scintillation and TEC measurements

from up to 10 GPS satellites in view above the horizon. CHAIN phase and amplitude scintillation data are measured at the L-band and are sampled at a rate of 50 Hz [Jayachandran et al., 2009]. A CHAIN GPS receiver and ionosonde are installed at Resolute Bay. This thesis attempts to analyze both L-band amplitude and phase data from CHAIN.

Chapter 2

METHODOLOGY

2.1 CERTO Phase Data Collection

CERTO data was provided by Dr. Carl Seifring and is available in a permanent repository at https://doi.org/10.5281/zenodo.3517195 [Siefring, 2018]. The CERTO data files are provided in text format with a .its file extension and, as such, can be opened in any text editor. Within these files we find 6 lines of header data and then a table containing the relevant data. The relevant information for this paper are are the data columns for VHF and UHF, along with some misc information in the header. This information will be observed in Section 2.3, where the concern for it is more pressing. In Listing 2.1, we can see an example of what a its file looks like. Another idiosyncrasy of these .its files is the original naming convention being a string with a standard format as "yyyyMMddHHmm" + 'r.its' with the "yyyyMMddHHmm" term being a time string displaying the year, month, day, hour, and minute of a time around the event and the 'r.its' with 'r' referring to data from Resolute Bay and '.its' being the file extension. The file's name time string can be found as the first text that appears on the first line of the files. For some files, this time string is the same as when the first data point is recorded, for others, such as in Listing 2.1 the time displayed is some time a few minutes before the first data point. We never discerned the reason for the file names and for ease of use we chose to rename the files with the exact time shown on the "First data point" line in the .its file, keeping the same

9

structure as "yyyyMMddHHmm" + 'r.its'.

```
2017-07-18 11:35 211 11:43:07.5  66.4 84.8 11:49  36 CASSIOPE       80
Station Coordinates: Resolute Bay    74.694 deg   -94.882 deg  365 m  -5 hrs
First data point @ 2017-07-18 11:38:26.43   ;   Data rate =   50 per sec
1 39265U 13055A   17196.58905696  .00004867  00000-0  14177-3 0  9999
2 39265  80.9711 345.6782 0687594 170.7403 190.7263 14.23019556195558
EndOfHeader
    VHF     VHF     UHF     UHF     L-B     L-B
      I       Q       I       Q       I       Q
     625   -1057      58       3      12       3     285
     519   -1090      59       3       5       1     287
     477   -1051      56      -1       5       4     286
```

Listing 2.1: Example .its file, 20170718113826r.its.

Analyzing CERTO data was challenging for a variety of reasons, initially stemming from the inability to use traditional methods for calculating σ_ϕ. The fundamental math behind filtering techniques and then calculating σ_ϕ is the issue. Traditionally, as with the CHAIN data set, σ_ϕ is calculated for data that last several hours long and interesting points within the time range are noted. What's important about that distinction is that events are not logged near the ends of the time series due to filtering artifacts that are present when processing the data. The regions of data referred to as artifacts are segments of prolonged rapid fluctuations. This wouldn't be a significant issue for CERTO's 20 minute long data sets if not for another problem with CERTO data itself. CERTO data contains flagged regions where the data is erroneous and cannot be used for any analysis, see Figure 2.3. These regions can be scattered anywhere within the CERTO data and may occur frequently for any length of time. In this section, we will be demonstrating the steps used to overcome these problems using one example data file that started collecting data on July 18th 2017 at 11:38:26 UTC and providing example plots of unsuccessful and successful filtering techniques in Figures 2.1-2.8.

Figure 2.1 shows a plot of the raw VHF phase from CERTO data. This example was chosen as it has some sections of flagged regions that end up splitting the data into two sections. This data also showcases an end on the left side that isn't flagged but, this still causes issues in filtering with a small time interval. The data also showcases an interesting region near the middle that we could imagine to be real scintillation,

such a sign of scintillation is rather uncommon to be intuitively visible from the raw phase data alone.
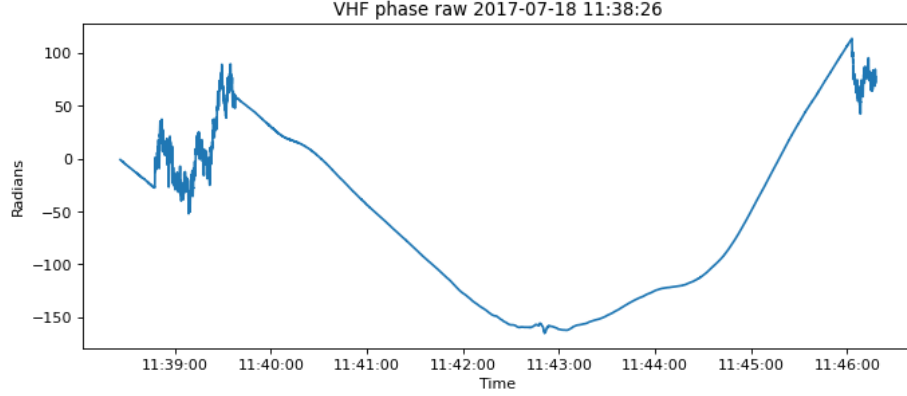
Figure 2.1: Raw VHF phase values from CERTO data from July 18th 2017 at 11:38:26.

In order to calculate either scintillation index we need to decide on a temporal average, also called a window. A window is a continuous set of data that is then averaged to calculate a scintillation index value. This process of windowing will mean that the resulting scintillation index will cover a shortened time range of the original data by a value of window length minus one. Since we are dealing with small time series in the CERTO data we have decided to choose a window length of 10 seconds of data, equating to 500 data points in a window at the original 50 Hz sample rate.

If we were to calculate σ_ϕ using the traditional detrending method outlined here,

- Third order polynomial fit to entire time series

- subtract polynomial fit from time series

- Linear detrending

- Apply zero-phase high pass filter with 6th order butterworth 0.1 Hz cutoff

and Equation 1.2 directly with the raw phase data, we would obtain what is shown in Figure 2.2. The clear issue with this is the regions of noise in the VHF phase raw plot that, when filtered and used to calculate σ_ϕ, provides the impression of strong scintillation in the region where the data are uncertain.
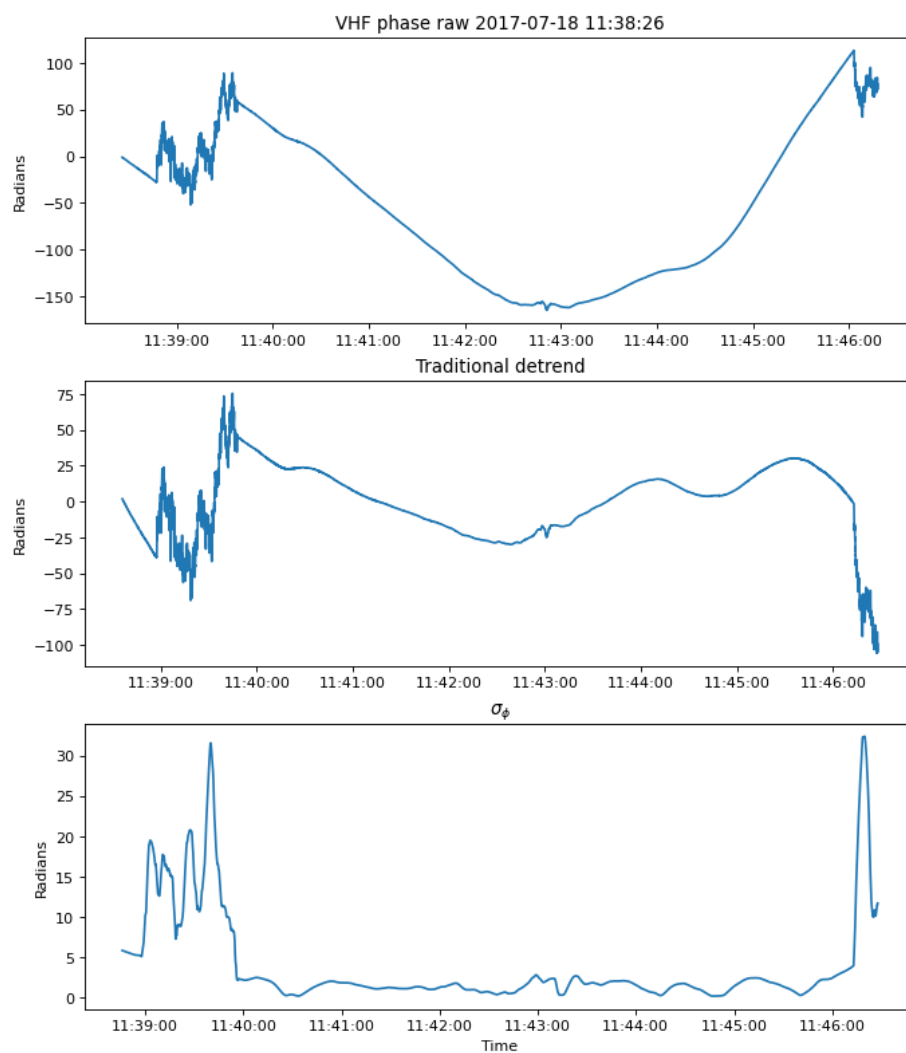
Figure 2.2: VHF phase data from CERTO detrended with the traditional detrending method with its calculated σ_ϕ values from July 18th 2017 at 11:38:26.

To get rid of these regions we rely on the .pro files that are included with the CERTO data. The pro files have the same file name as their corresponding its files. For our purposes, these pro files store values for CERTO data that update by the second with a flag number that is either 0 for data with no issues, or a number higher than 0 that means the data has problems during the time. Something important to note is that the .pro files always end up having at least some data at the end of the file with values greater than 0. Since the .pro files update a second at a time we need to repeat each data point 50 times to match the 50 Hz CERTO data. The start of an example pro file can be seen in Listing 2.2. The flag data are shown under the UHF, VHF, and phase flag columns.

```
0 2017-07-18 11:35 211 11:43:07.5  66.4 84.8 11:49  36 CASSIOPE        80
  Station Coordinates: Resolute Bay    74.694 deg   -94.882 deg  365 m  -5 hrs
  First data point @ 2017-07-18 11:38:26.00   ;   Data rate =   50 per sec
  1 39265U 13055A   17196.58905696  .00004867  00000-0  14177-3 0  9999
  2 39265  80.9711 345.6782 0687594 170.7403 190.7263 14.23019556195558
5 EndOfHeader
    Time    Rel TEC   UHF  VHF phase   Az      El    Flat     Flon     Elat     Elon
    (sec)   (10^16)  flag flag flag  (deg)   (deg)  (deg)    (deg)    (deg)    (deg)
            (el/m^2)
     1.00    3.977    0    0     0   211.92  17.01  67.184 -106.176  71.747 -100.401
10   2.00    3.952    0    0     0   211.92  17.20  67.248 -106.111  71.777 -100.353
     3.00    3.925    0    0     0   211.92  17.30  67.279 -106.081  71.791 -100.330
```

Listing 2.2: Example .pro file, 20170718113826r.pro.

From here on, we will refer to the data within the .pro files as the flagged data. At this point, the CERTO data may have a few more data points in it than the flagged data and since the flagged data are always 0 at the end we can just cut off the few extra data points from the CERTO file. The result of this effort is shown in Figure 2.3.

Our first idea we had to remove the undesirable regions from the raw phase was to apply a 6th order 0.1 Hz butterworth filter to the raw data directly and then calculate the resulting σ_ϕ directly. This technique didn't work on it's own as shown in Figure 2.4. Had this technique worked on it's own it likely wouldn't have produced desirable results because these undesirable fluctuations are in the band-pass of the filter and removing them would have also removed the real scintillation events we are
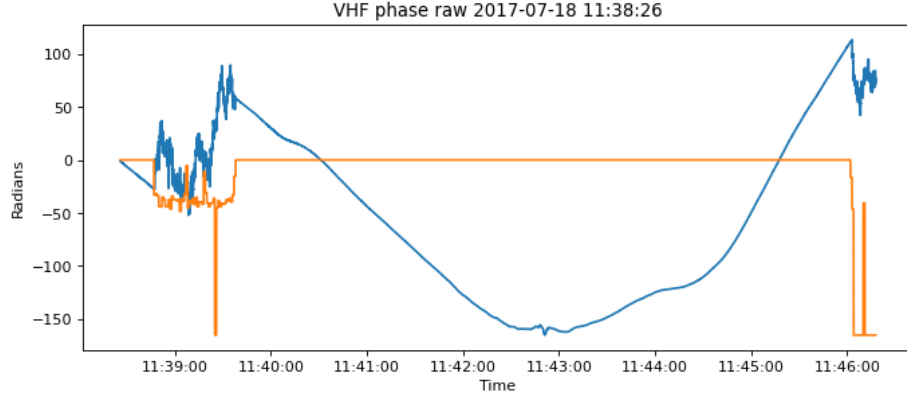
Figure 2.3: The same raw VHF phase data shown in Figure 2.1 with the flagged region shown in orange. The flagged data has been normalized to the VHF phase data for visual clarity for this image.

attempting to isolate.

Next, we attempted to linearly interpolate the data backwards from the starting values at the beginning of the VHF raw phase data while setting the VHF phase data that corresponded to the flagged data to NaN values. The purpose of the linear interpolation was to pad the edges of the data so that the filtered data would contain the same number of points as the raw data. The reason the flagged data was set to NaN was to remove the flagged region in the filtered and σ_ϕ data. We then used the same butterworth filter from before and calculated σ_ϕ. While doing this we noticed that removing only the flagged data region didn't eliminate the noise from the resulting plots. In an attempt to mitigate this issue, we removed an additional half of a window and a full window worth of extra data on both sides of the flagged region. This resulted in what is shown in Figure 2.5. The beginning linear interpolation, while not shown on the plot, consisted of 3000 data points backwards linearly interpolated from the first two points of raw VHF phase data. The first plot shows the raw VHF phase data with the flagged data regions plotted over it with an extra half window and extra full window width to show how far the data are being removed. The second row of plots shows the full window removal butterworth filtered data and resulting σ_ϕ. The third row shows the same but with the half window removed and the last row shows how this compares to what was shown in Figure 2.4. This effort was not
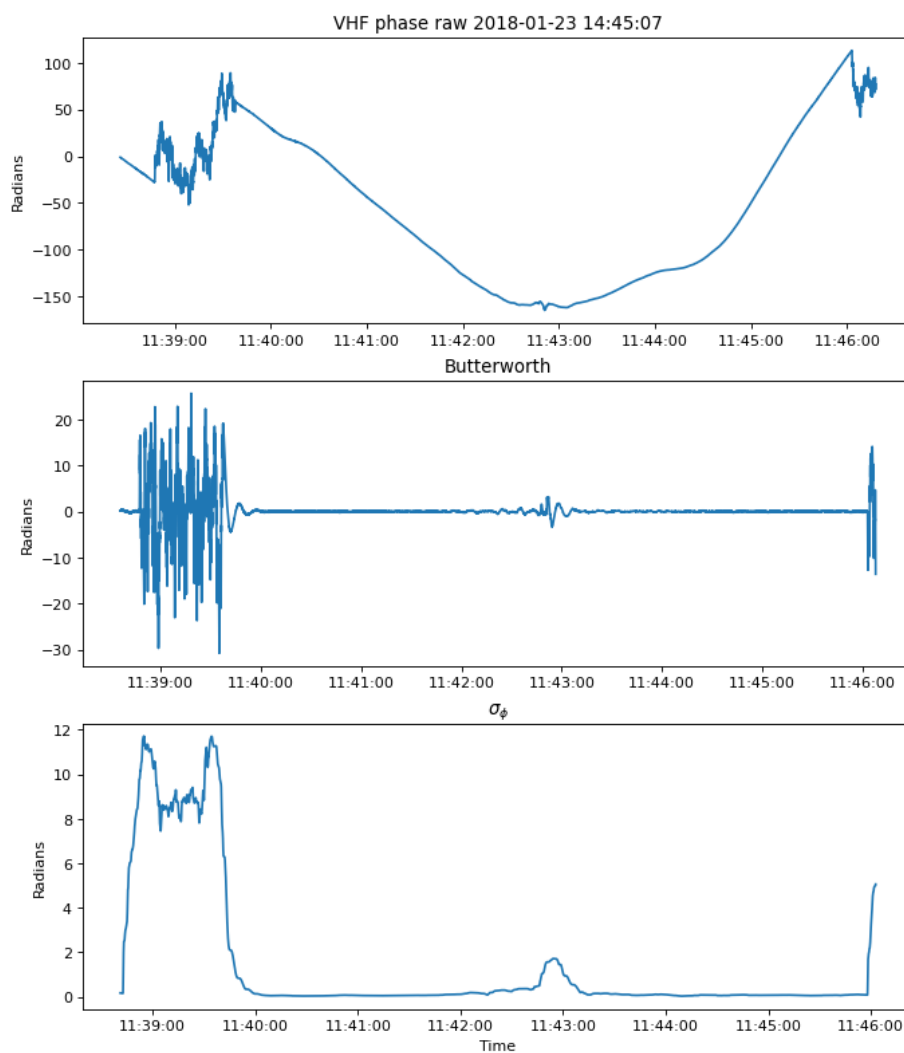
Figure 2.4: VHF phase data from CERTO filtered with a sixth order butterworth filter at 0.1 Hz with its calculated σ_ϕ values from July 18$^{\text{th}}$ 2017 at 11:38:26.

very fruitful as can be shown in the resulting σ_ϕ values featuring a gap that removes most, but not all of the erroneous data.

Our next effort was to create a linear interpolation over the flagged region of data, creating a moving average of that linear interpolation, and subtracting the interpolated region by the moving average, then using the same butterworth filter and calculation for σ_ϕ. This can be seen in Figure 2.6. This had the most promising result so far but this method will always create peaks at the start and end of the interpolated regions due to the moving average being smooth and the linear interpolation being sharp at these points.

We tried to split the data into different time ranges by separating using the flag data. These new 'time splits' were analyzed independently of each other. The time splits were based on a half window larger than the range of the flags covered over the raw data. We checked the resulting time splits to ensure they were larger than 20 seconds, an arbitrary decision based on double the size of our windowing choice of 10 seconds. With the time splits we created a moving average, subtracted that from the raw data, deleted a half a window of additional data from the ends of the flagged region, added half a window of zeros to pad the data at both ends, filtered the data with a 6th order 0.1 Hz butterworth filter, removed a full window from both ends, and calculated σ_ϕ from that. This result can be seen in Figure 2.7.

We then did the same method as above, but instead of zero padding we used a Gaussian distribution of noise centered at zero with a standard deviation of 1 as padding. This was done due to a concern of creating a discontinuity from the zero padding instead of variable data. The results of this effort seen in Figure 2.8 show fairly unnoticeable differences at the far ends of the resulting σ_ϕ when compared to Figure 2.7.
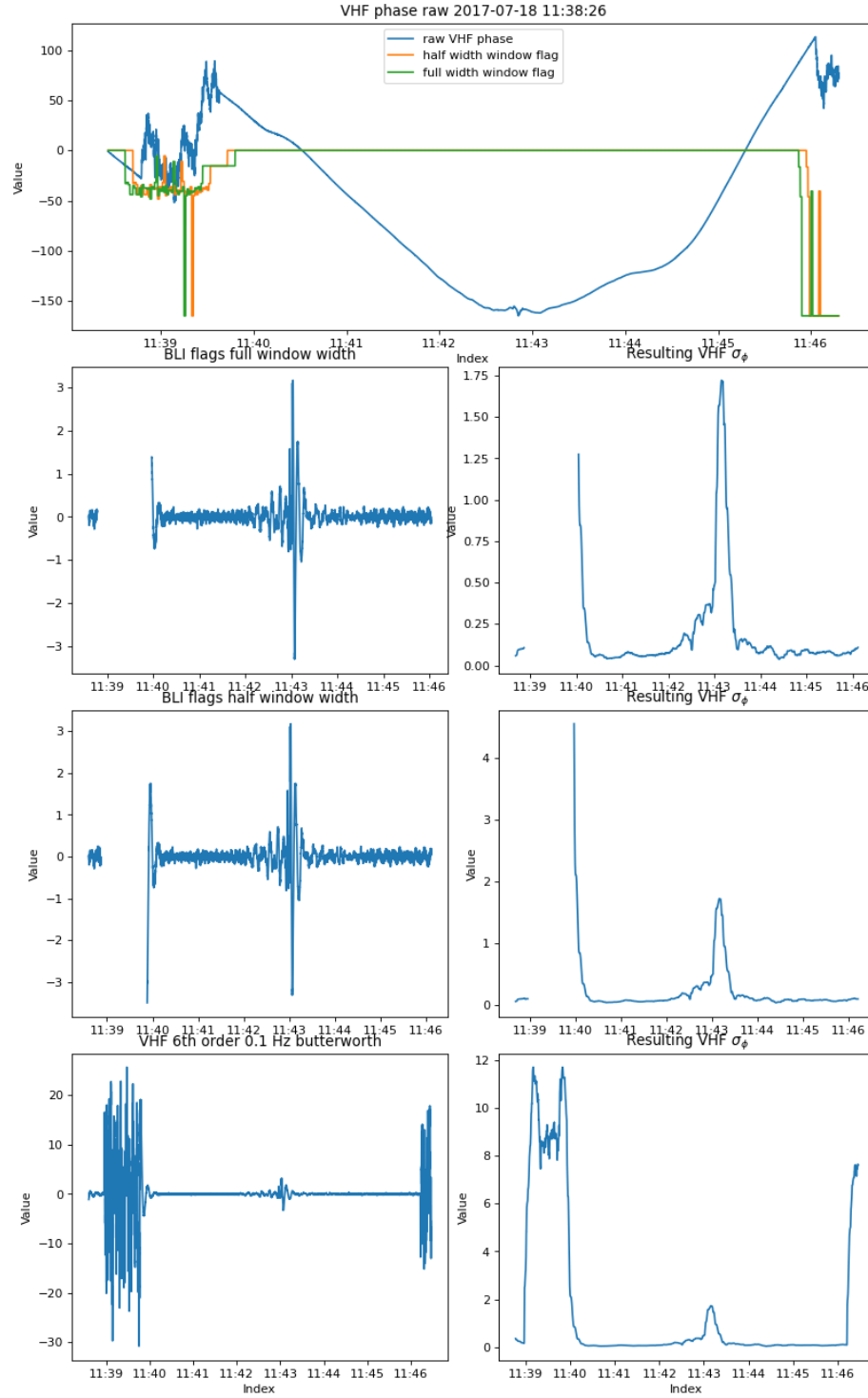
Figure 2.5: VHF phase data from CERTO with flagged regions removed with an additional full window and half window worth of data removed. The plot shown on the bottom row here is identical to the one shown in Figure 2.4.
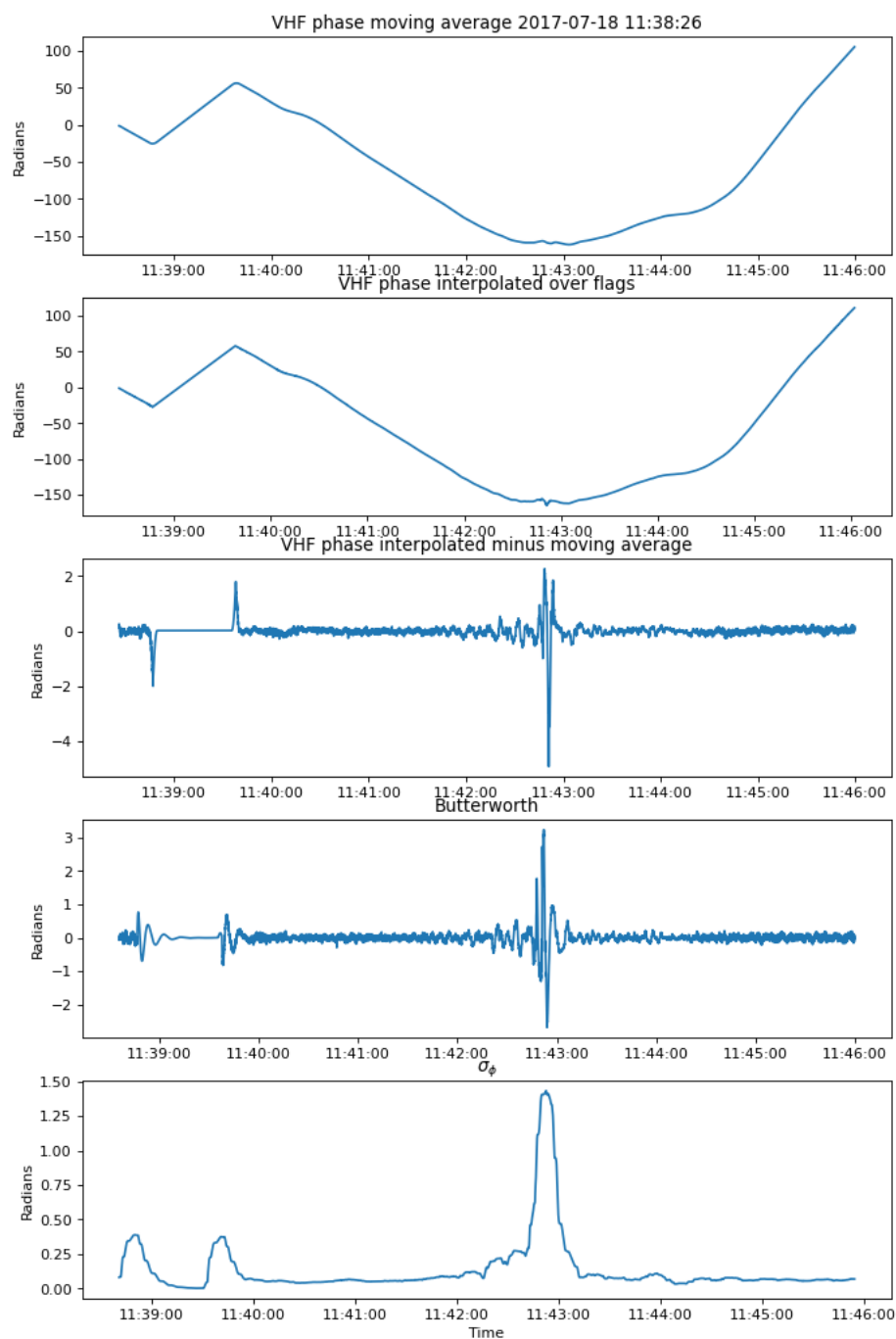
Figure 2.6: Plotted moving average of VHF phase data from CERTO interpolated over flagged regions.
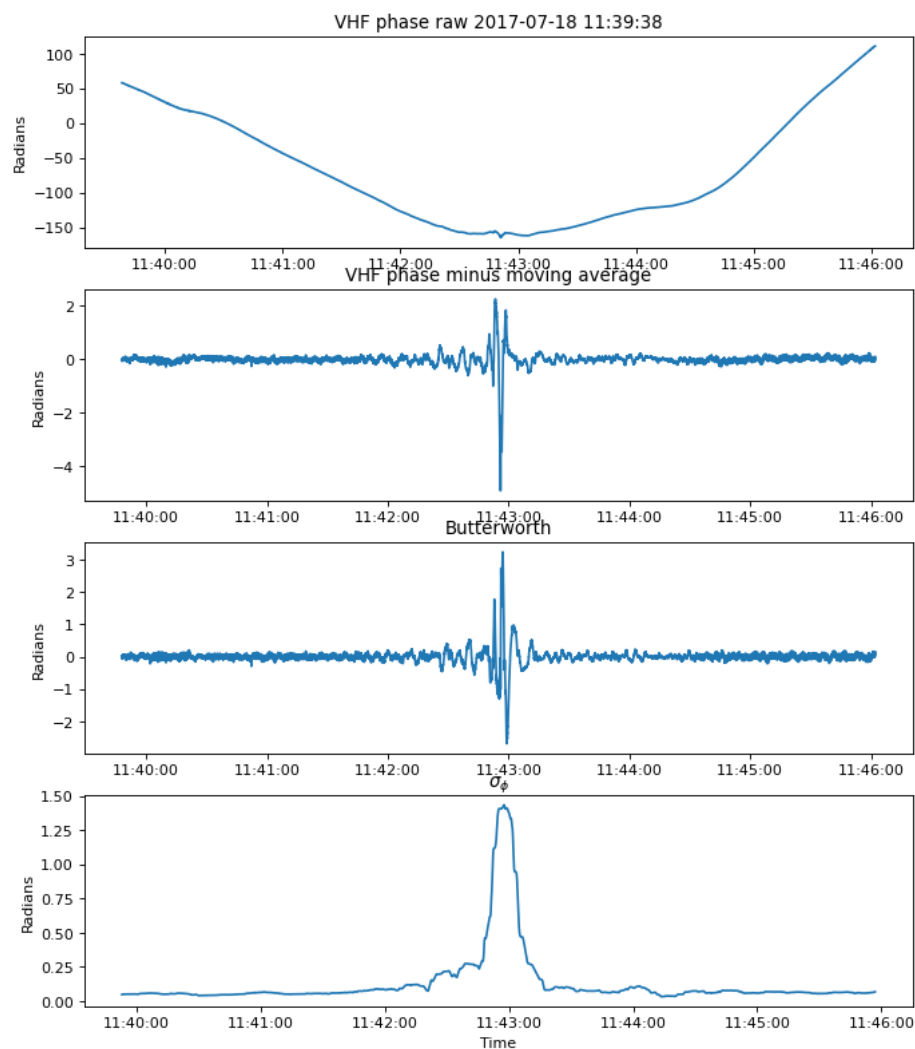
Figure 2.7: VHF phase data from CERTO with a full window padding of zeros, not pictured, on the VHF phase minus moving average. The resulting filtered and σ_ϕ data are shown.
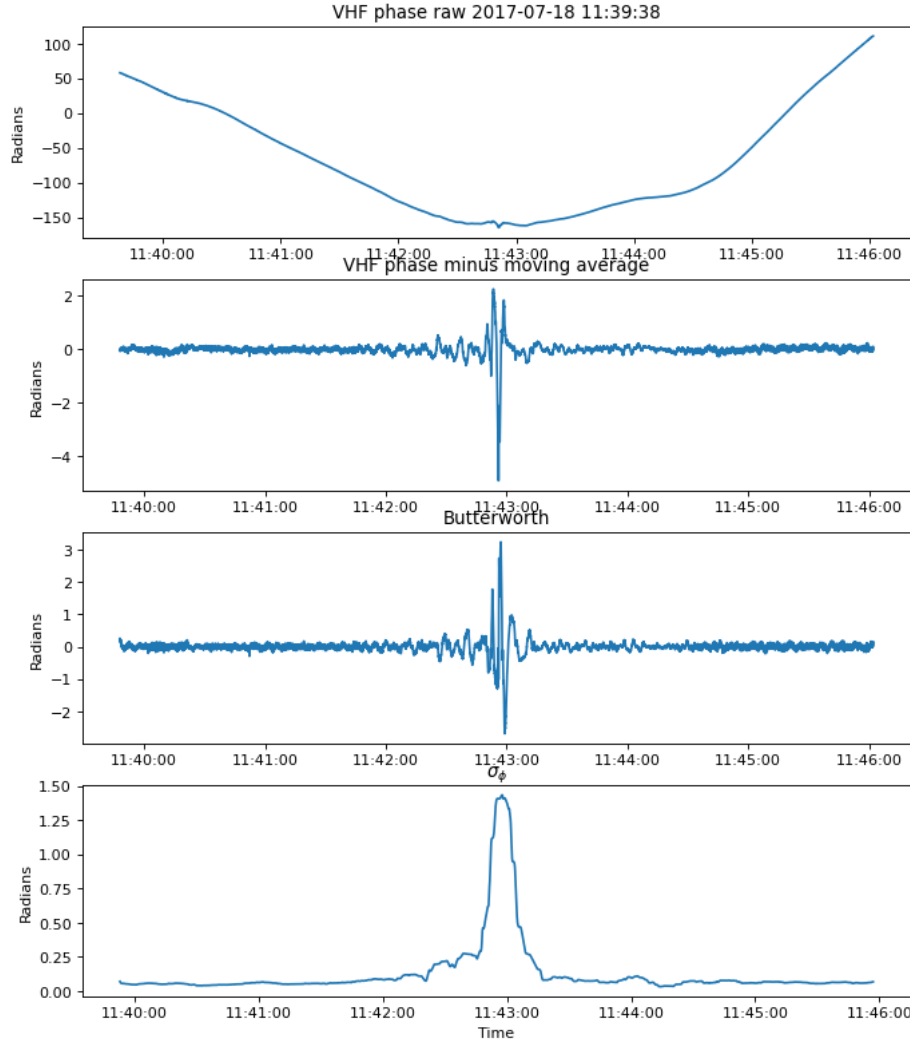
Figure 2.8: VHF phase data from CERTO with a full window padding of a Gaussian distribution of noise, not pictured, on the VHF phase minus moving average. The resulting filtered and σ_ϕ data are shown.

2.2 CHAIN Data Collection

The CHAIN data are obtained from the Canadian High Arctic Ionospheric Network's online website at http://chain.physics.unb.ca/chain/pages/data_{}download.

We based the acquisition of CHAIN data on matching the CERTO time frames from the same CERTO data from the earlier section. This was a non trivial process

and we will start with what the CHAIN data are. CHAIN data files are stored as a binary format which is parsed and converted to a HDF5 file organized by hour. These files contain data on all PRN satellites that were active during the hour. The relevant data of concern are the UTC, phase, and power data as can be seen in Figure 2.9.
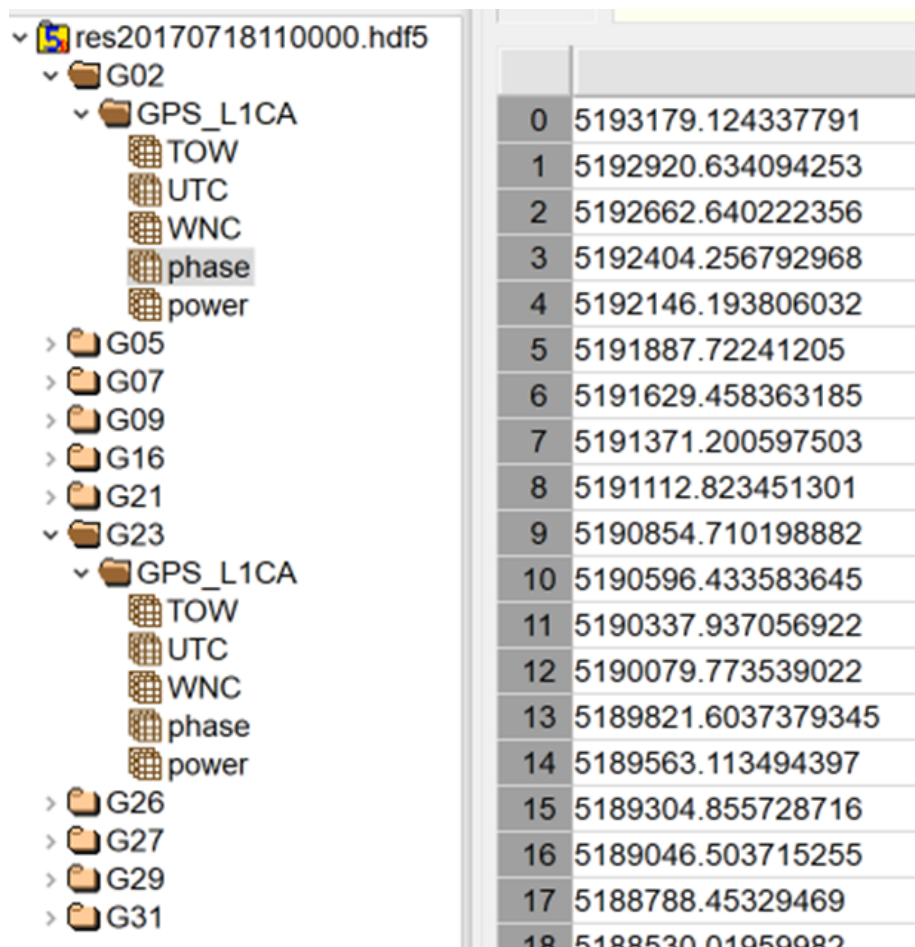
Figure 2.9: The file structure of a normal chain HDF5 file, shown left, res20170718110000.hdf5. The beginning values of the highlighted phase data are also displayed, shown right.

We need to perform 3 checks to ensure that the CHAIN data for each satellite is usable:

1. Satellite PRN data must exist within all time frames

- – If the CERTO time covers multiple whole hour times we can eliminate satellites that only exist in one hour but not the other

2. Satellite PRN data must contain CERTO start and end times

   - – If the satellites UTC time does not contain the CERTO start or end time we can eliminate it

3. Satellite PRN data must contain continuous data

   - – In the event that the satellite exist within the start and end time but is missing data within the time series we eliminate it

Once we have a list of all the CHAIN PRN's that have data matching the CERTO data we can gather the data and conduct our analysis.

For calculating σ_ϕ for the CHAIN data we use the traditional detrending method outlined in Section 2.1 along with the same σ_ϕ calculation seen in Equation 1.2. The reason we use the traditional method is that is because of the way σ_ϕ is calculated, it leaves the edges of the data erroneous. The size of this error is dependent on the size of the windowing used for the computation. This isn't an issue with the CHAIN data as satellite passes are last for several hours while the CERTO passes are at most 20 minutes in length. The CERTO data also possesses flagged sections of data which only serves to compound the issue by creating smaller continuous time regions of data. The way we're observing CHAIN data within this paper doesn't fall into any meaningful issues over concern with the edges of the data. Because of this, we may also observe CHAIN power data, unlike with the CERTO data. Since the CHAIN data has no complications we can use the traditional method of detrending the data. The power detrending algorithm is shown here.

- • Apply a zero-phase low pass 6th order Butterworth filter with a 0.1 Hz cutoff

- • Divide original signal by the previous step

This should provide a detrended power signal centered around 1 in dB. This detrended power is used with Equation 1.1 to calculate S_4.

2.3 Creating Satellite Conjunctions with CHAIN and CERTO

For this project we decided to observe CERTO and CHAIN events that were close in proximity for the purpose of multi-frequency scintillation analysis in the polar caps. To judge if a satellite was close enough we chose a 15° angular separation between satellites maintained for a minimum of 10 seconds of continuous data. 147 events were obtained from this method and σ_ϕ comparison plots were made. To determine the angular separation between satellite we used the Haversine formula,

$$\theta = 2 \arcsin\left(\sqrt{\sin^2\left(\frac{\varphi_2 - \varphi_1}{2}\right) + \cos\varphi_1 \cdot \cos\varphi_2 \cdot \sin^2\left(\frac{\lambda_2 - \lambda_1}{2}\right)}\right). \quad (2.1)$$

where θ is the angular separation between satellites, φ is the elevation of the satellite relative to Resolute Bay, λ is the azimuth of the satellite relative to Resolute Bay, and the subscripts 1 & 2 are interchangeably either the satellite from CHAIN or CERTO. Because of the way we calculate the angular separation we need to gather a continuous data series of the elevation and azimuth angles for both the CERTO and CHAIN satellites.

2.3.1 Gathering CERTO Satellite Properties

The pro files do give the elevation and azimuth angles of the satellites for all of the data we would need. However, the pro files only update every second while the data we want to have should update at 50 Hz. We can instead use the TLE found in either the pro file or the its file as seen in Listing 2.1, which can be found on lines 3-4 and be used to propagate satellite properties with some python package like Skyfield https://pypi.org/project/skyfield/. Because of this, the CERTO data are propagated through to find the elevation angle relative to CERTO at Resolute Bay.

2.3.2 Gathering CHAIN Satellite Properties

The CHAIN data doesn't possess anything like TLEs within the HDF5 files in a similar way the CERTO data has, so we need to rely on an alternative way of getting the satellite TLEs. The PRNs inside of each HDF5 file correspond to a trackable satellite within the database here https://www.space-track.org. A table of this data is presented in Table 2.1. PRNs change whenever a satellite goes out of commission and is then eligible to be used again. Because of this, the PRN alone isn't enough to determine the satellite, we also need to know when the satellite was active. The HDF5 files provide the UTC time in seconds which we can use to find the date the event occurred and then use Table 2.1 to find the NORAD ID associated with the PRN. Then we use the Space-Track api and the UTC at the beginning of the time series to fetch a TLE closest to the event. This TLE is propagated with the python package Skyfield and the elevation and azimuth angles are obtained.

Table 2.1: CHAIN satellite PRNs with COSPAR & NORAD IDs and effective start and end dates for viewing TLEs with the Space-Track api.

#	COSPAR	NORAD	SY	SM	SD	SH	SM	SS	EY	EM	ED	EH	EM	ES
1	1992-079A	22231	1992	11	22	00	00	00	2008	10	17	00	00	00
1	1993-032A	22657	2008	10	23	00	00	00	2009	01	07	00	00	00
1	2009-014A	34661	2009	03	24	00	00	00	2011	05	07	00	00	00
1	1993-054A	22779	2011	06	02	00	00	00	2011	07	13	00	00	00
1	2011-036A	37753	2011	07	16	00	00	00						
2	1989-044A	20061	1989	06	10	00	00	00	2004	05	13	00	00	00
2	2004-045A	28474	2004	11	06	00	00	00						
3	1985-093A	16129	1985	10	09	00	00	00	1994	04	14	00	00	00
3	1996-019A	23833	1996	03	28	00	00	00	2014	08	19	00	00	00
3	1993-054A	22779	2014	09	05	00	00	00	2014	10	21	00	00	00
3	2014-068A	40294	2014	10	29	00	00	00						
4	1978-020A	10684	1978	02	22	00	00	00	1985	07	18	00	00	00
4	1993-068A	22877	1993	10	26	00	00	00	2015	11	09	23	59	59
4	2009-014A	34661	2016	02	02	00	00	00	2016	09	14	00	00	00
4	1992-079A	22231	2016	09	15	00	00	00	2016	12	06	00	00	00
4	1993-068A	22877	2016	12	09	00	00	00	2017	01	04	00	00	00
4	2009-014A	34661	2017	01	06	00	00	00	2017	05	13	00	00	00
4	1997-067A	25030	2017	05	19	00	00	00	2017	07	14	23	59	59
4	1994-016A	23027	2017	07	20	00	00	00	2017	11	28	23	59	59
4	2009-014A	34661	2017	12	01	00	00	00	2018	09	29	00	00	00
4	1994-016A	23027	2018	10	10	00	00	00	2019	01	03	00	00	00
4	2018-109A	43873	2019	01	09	00	00	00	2019	07	13	00	00	00
4	1994-016A	23027	2019	07	13	00	00	00	2019	10	08	23	59	59
4	2018-109A	43873	2019	10	21	00	00	00						
5	1980-011A	11690	1980	02	09	00	00	00	1984	05	12	00	00	00
5	1993-054A	22779	1993	08	30	00	00	00	2009	06	09	00	00	00
5	2009-043A	35752	2009	08	17	00	00	00						
6	1978-093A	11054	1978	10	06	00	00	00	1992	05	19	00	00	00
6	1994-016A	23027	1994	03	10	00	00	00	2014	03	04	00	00	00

Table 2.1: CHAIN satellite PRNs with COSPAR & NORAD IDs and effective start and end dates for viewing TLEs with the Space-Track api.

#	COSPAR	NORAD	SY	SM	SD	SH	SM	SS	EY	EM	ED	EH	EM	ES
6	2009-014A	34661	2014	04	03	00	00	00	2014	05	06	00	00	00
6	2014-026A	39741	2014	05	17	00	00	00						
7	1978-047A	10893	1978	05	13	00	00	00	1988	02	13	00	00	00
7	1993-032A	22657	1993	05	13	00	00	00	2008	01	15	00	00	00
7	2008-012A	32711	2008	03	15	00	00	00						
8	1978-112A	11141	1978	12	10	00	00	00	1989	10	15	00	00	00
8	1997-067A	25030	1997	11	06	00	00	00	2015	04	14	00	00	00
8	2009-014A	34661	2015	04	30	00	00	00	2015	07	02	00	00	00
8	2015-033A	40730	2015	07	15	00	00	00						
9	1980-032A	11783	1980	04	26	00	00	00	1991	03	07	00	00	00
9	1993-042A	22700	1993	06	26	00	00	00	2014	07	22	00	00	00
9	2014-045A	40105	2014	08	02	00	00	00						
10	1996-041A	23953	1996	07	16	00	00	00	2015	08	04	00	00	00
10	1994-016A	23027	2015	09	16	00	00	00	2015	10	27	00	00	00
10	2015-062A	41019	2015	10	31	00	00	00						
11	1983-072A	14189	1983	07	14	00	00	00	1993	05	05	00	00	00
11	1999-055A	25933	1999	10	07	00	00	00	2021	06	16	23	59	59
11	2021-054A	48859	2021	06	17	00	00	00						
12	1984-097A	15271	1984	09	08	00	00	00	1996	03	28	00	00	00
12	2006-052A	29601	2006	11	17	00	00	00						
13	1984-059A	15039	1984	06	13	00	00	00	1994	06	21	00	00	00
13	1997-035A	24876	1997	07	23	00	00	00						
14	1989-013A	19802	1989	02	14	00	00	00	2000	04	16	00	00	00
14	2000-071A	26605	2000	11	10	00	00	00	2020	11	04	23	59	59
14	2020-078A	46826	2020	11	05	00	00	00						
15	1990-088A	20830	1990	10	01	00	00	00	2007	03	14	00	00	00
15	2007-047A	32260	2007	10	17	00	00	00						
16	1989-064A	20185	1989	08	18	00	00	00	2000	10	14	00	00	00
16	2003-005A	27663	2003	01	29	00	00	00						
17	1989-097A	20361	1989	12	11	00	00	00	2005	02	24	00	00	00
17	2005-038A	28874	2005	09	26	00	00	00						
18	1990-008A	20452	1990	01	24	00	00	00	2000	08	19	00	00	00
18	2001-004A	26690	2001	01	30	00	00	00	2018	01	23	23	59	59
18	1993-068A	22877	2018	01	24	00	00	00	2020	03	09	23	59	59
18	2019-056A	44506	2020	03	13	00	00	00						
19	1989-085A	20302	1989	10	21	00	00	00	2001	09	12	00	00	00
19	2004-009A	28190	2004	03	20	00	00	00						
20	1990-025A	20533	1990	03	26	00	00	00	1996	12	14	00	00	00
20	2000-025A	26360	2000	05	11	00	00	00						
21	1990-068A	20724	1990	08	02	00	00	00	2003	01	28	00	00	00
21	2003-010A	27704	2003	03	31	00	00	00						
22	1993-007A	22446	1993	02	03	00	00	00	2003	08	07	00	00	00
22	2003-058A	28129	2003	12	21	00	00	00						
23	1990-103A	20959	1990	11	26	00	00	00	2004	02	17	00	00	00
23	2004-023A	28361	2004	06	23	00	00	00	2020	06	09	23	59	59
23	2020-041A	45854	2020	07	14	00	00	00						
24	1991-047A	21552	1991	07	04	00	00	00	2011	10	01	00	00	00
24	2009-014A	34661	2012	02	02	00	00	00	2012	03	14	23	59	59
24	1992-079A	22231	2012	03	15	00	00	00	2012	04	25	23	59	59
24	1993-032A	22657	2012	04	26	00	00	00	2012	05	31	00	00	00
24	2009-014A	34661	2012	08	09	00	00	00	2012	08	23	00	00	00
24	2012-053A	38833	2012	10	04	00	00	00						
25	1992-009A	21890	1992	02	23	00	00	00	2010	02	08	23	59	59
25	1993-054A	22779	2010	02	09	00	00	00	2010	05	27	23	59	59
25	2010-022A	36585	2010	05	28	00	00	00						
26	1992-039A	22014	1992	07	07	00	00	00	2015	01	06	00	00	00

Table 2.1: CHAIN satellite PRNs with COSPAR & NORAD IDs and effective start and end dates for viewing TLEs with the Space-Track api.

#	COSPAR	NORAD	SY	SM	SD	SH	SM	SS	EY	EM	ED	EH	EM	ES
26	1992-079A	22231	2015	02	05	00	00	00	2015	02	25	00	00	00
26	1992-058A	22108	2015	02	27	00	00	00	2015	03	17	00	00	00
26	2015-013A	40534	2015	03	25	00	00	00						
27	1992-058A	22108	1992	09	09	00	00	00	2012	10	17	23	59	59
27	2009-014A	34661	2012	10	18	00	00	00	2013	05	10	00	00	00
27	2013-023A	39166	2013	05	15	00	00	00						
28	1992-019A	21930	1992	04	10	00	00	00	1997	08	16	00	00	00
28	2000-040A	26407	2000	07	16	00	00	00						
29	1992-089A	22275	1992	12	18	00	00	00	2007	10	24	00	00	00
29	2007-062A	32384	2007	12	20	00	00	00						
30	1996-056A	24320	1996	09	12	00	00	00	2011	08	04	23	59	59
30	1993-054A	22779	2011	08	05	00	00	00	2013	05	07	00	00	00
30	2009-014A	34661	2013	05	10	00	00	00	2013	08	21	23	59	59
30	1992-079A	22231	2013	08	22	00	00	00	2013	09	16	23	59	59
30	1993-032A	22657	2013	09	19	00	00	00	2013	10	08	00	00	00
30	1992-058A	22108	2013	12	03	00	00	00	2013	12	17	23	59	59
30	2009-014A	34661	2013	12	19	00	00	00	2014	02	10	23	59	59
30	2014-008A	39533	2014	02	21	00	00	00						
31	1993-017A	22581	1993	03	30	00	00	00	2005	10	25	00	00	00
31	2006-042A	29486	2006	09	25	00	00	00						
32	1990-103A	20959	2006	12	02	00	00	00	2016	01	25	23	59	59
32	2016-007A	41328	2016	02	05	00	00	00						

Chapter 3

Results

3.1 CERTO and CHAIN Satellite Conjunctions

Figure 3.1 is an example plot of a conjunction event. In it, the red and orange circles are the IPPs of the CERTO and CHAIN satellites, respective. The satellite locations are shown to illustrate the necessity of utilizing the IPP to compare proximity, as shown by the CHAIN satellite which is across the world over Russia. The physical location of the satellites will always differ greatly due to the CERTO satellites orbiting in LEO and the CHAIN satellites orbiting in GEO.

3.1.1 σ_ϕ Plot Comparison

An example conjunction comparison of the σ_ϕ scintillation data is shown in Figure 3.2. This plot is the data during the event shown in the IPP plot in Figure 3.1. As the minimum time set to count as a conjunction was set at 10 seconds, a majority of events ended up lasting for this amount of time and coincidentally lack significant scintillations.

Figure 3.3 shows an example of the raw phase values for both the VHF and L-band data used to calculate σ_ϕ. This figure is here to show the fundamental differences in the shape and scale of the average CERTO and CHAIN raw phase data. This data contains the data used for calculating the σ_ϕ data displayed in Figure 3.2.
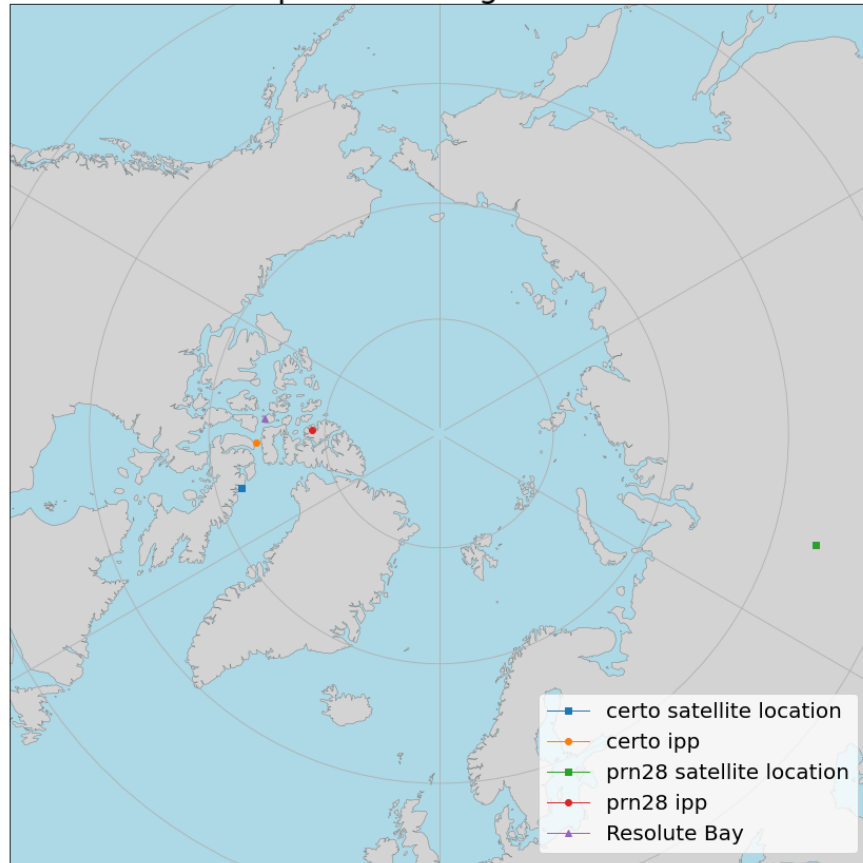
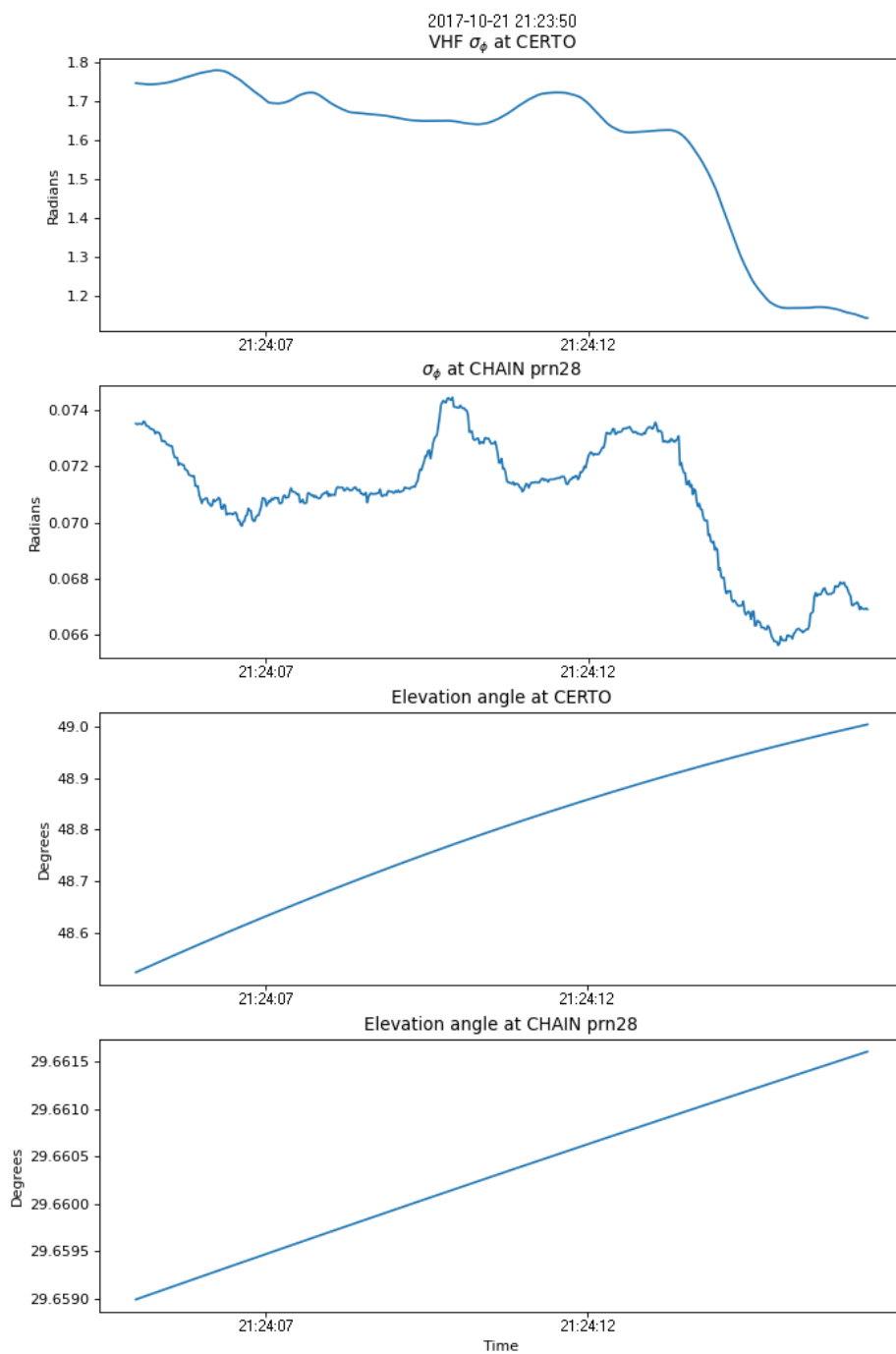Figure 3.1: Plots of ionospheric pierce points of satellites and there relative locations above Earth.

Figure 3.2: Example plot of σ_ϕ and elevation angle for event shown in Figure 3.1.
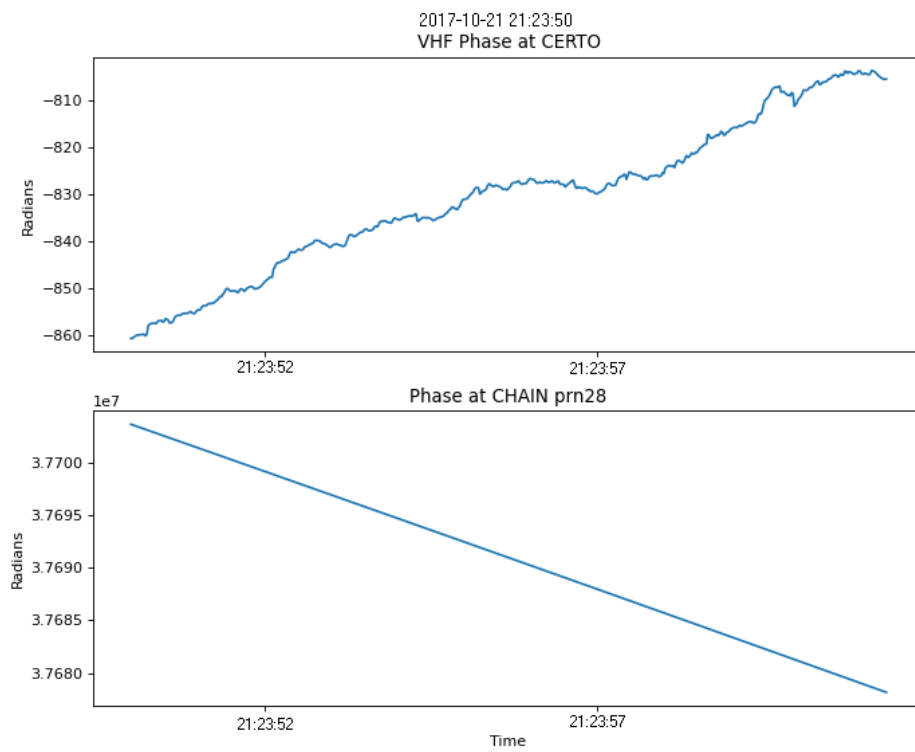
Figure 3.3: Example plot of raw values for phase used to calculated the data shown in Figure 3.2.

3.1.2   RISR Data

Of the 147 conjunctions, we found 15 that occurred while RISR was collecting data. Figure 3.4 shows plotted electron density RISR data taken during the example conjunction above. The other 15 conjunctions are displayed in Appendix A. Most of the conjunctions did not have significant scintillations regardless of whether or not they were located inside of density enhancements. The plot in Figure 3.4 is created from two RISR experiments to show the electron density before the event on October, 21th 2017 at 21:23:50.94, shown near the start of the second part of the experiment. As RISR isn't continuously operational at any given time, the data shown in Figure 3.4 shows a white space where RISR was not operational.
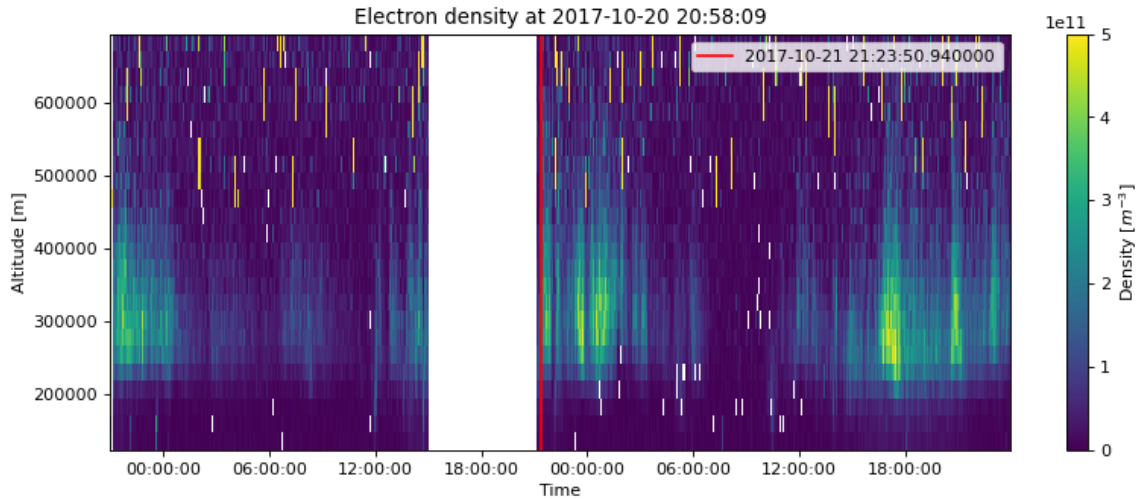
Figure 3.4: RISR electron density from near vertical beam

3.2   Histograms

Histograms detailing the total results of all scintillation data from VHF and L-band frequencies are presented in the plots of this section. An individual data point of scintillation is the result of a window's width, 10 seconds, of data calculated from the initial raw data. The purpose of these histograms is to view the overall distribution of scintillation in the polar cap to gain insight into the occurrence rate of irregularities at

VHF Fresnel scales (~1 km) compared to L-band Fresnel scales (~250 m). The VHF histograms plot all calculated σ_ϕ values obtained from every CERTO data file. The L-band histograms plot all available data from the CHAIN database that matched the duration and time frame as the CERTO data. The majority of all σ_ϕ scintillation values from both VHF and L-band are low as the bulk of the data collected is over quiet regions in the ionosphere with minimal or no structuring. The S_4 values for the L-band histogram similarly consist of mostly low values. Figures 3.5, 3.6, & 3.7 show differing views of VHF σ_ϕ histograms, while Figures 3.8, 3.9, 3.10, & 3.11 show differing views of L-band S_4 and σ_ϕ plots. At the tail end of the VHF σ_ϕ histogram shown in Figure 3.7 we see large clustering of data at single values, which implies that these are the values likely capture phenomenon responsible for strong scintillation as opposed to random noise within the data causing perceived strong scintillation or an error in the data analysis. The events responsible for this higher values of scintillation are shown in Section 3.3.3. The tail end in Figure 3.9 shows the counts of unrealistically high values for scintillation data compared to values presented in literature such as [Pan and Yin, 2014]. As such, we believe these values to be false and potentially an expected consequence of such a large data set, i.e. rare edge case artifacts that were overlooked despite efforts to sanitize the dataset. The L-band σ_ϕ normal for a scintillation distribution in the restricted range of 0-0.3 chosen for Figure 3.10, but viewing the whole distribution with a log scaled y-axis in Figure 3.11 we can see a non-trivial amount of data with values well above anything in the published literature and so we speculate that these may not be representative of actual strong scintillations.

3.3   CERTO σ_ϕ

3.3.1 σ_ϕ Scintillation Peaks Corresponding to High Elevation Angles

A recent modeling of electromagnetic wave propagation called Satellite-beacon Ionospheric-scintillation Global Model of the upper Atmosphere (SIGMA) used to simulate GNSS
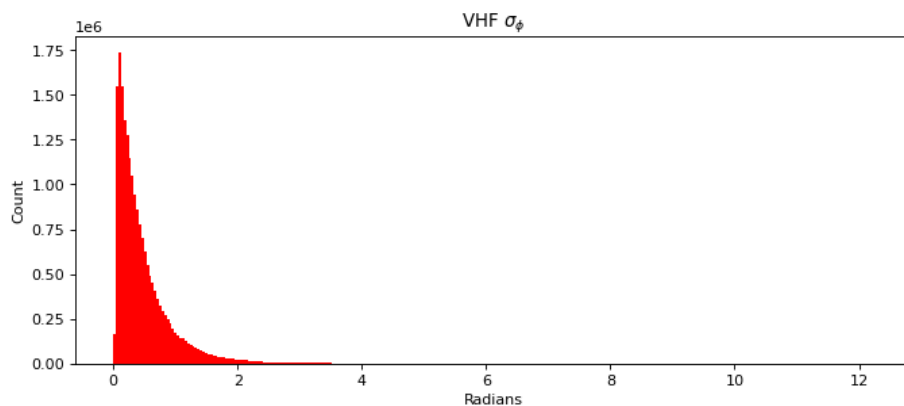
Figure 3.5: Histogram of all total VHF σ_ϕ scintillation data.
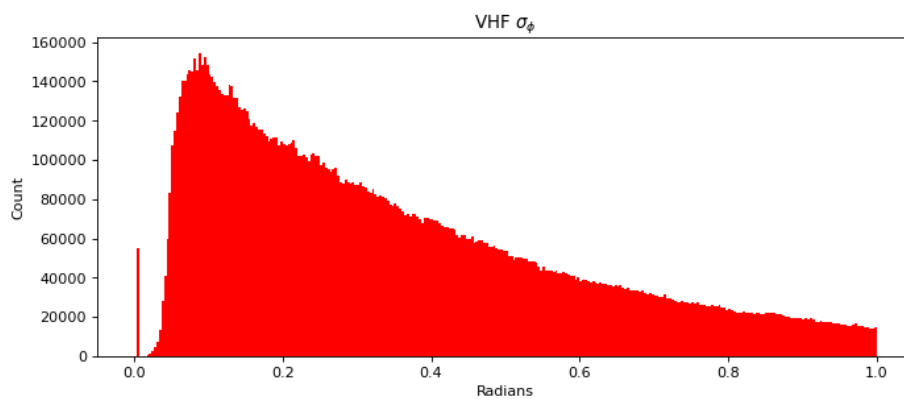
Figure 3.6: Focused view of VHF σ_ϕ scintillation with σ_ϕ between 0 and 1. Same data as shown in Figure 3.5.
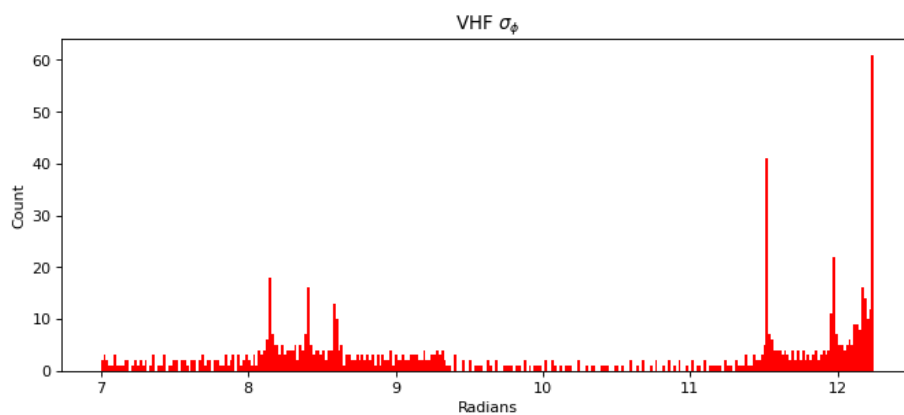
Figure 3.7: Viewing the tail end of the VHF σ_ϕ histogram shows us that there are multiple high values tailing off the plot instead of one singular instants of high values.

Figure 3.8: Histogram of all total L-band S_4 scintillation data with the x-axis scaled from 0-0.3.

Figure 3.9: Viewing the tail end of the L-band S_4 histogram shows us that there very few extreme values that are likely some sort of error.

Figure 3.10: Histogram of all total L-band σ_ϕ scintillation data with the x-axis scaled from 0-0.3.

Figure 3.11: A log scaled plot of the L-band σ_ϕ scintillation data.

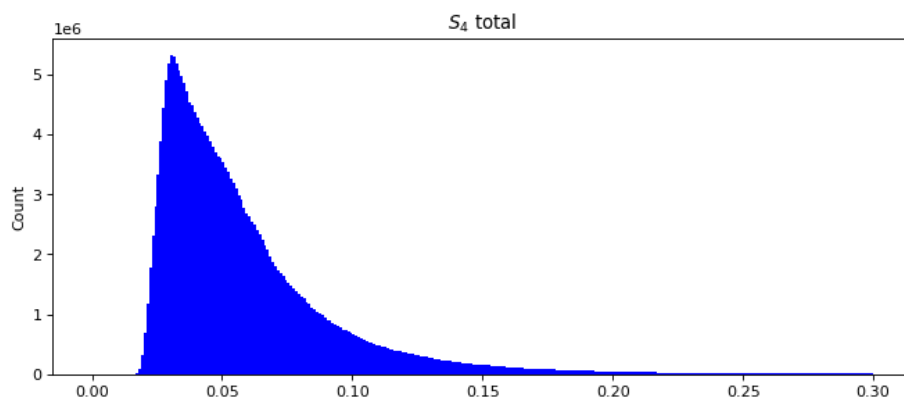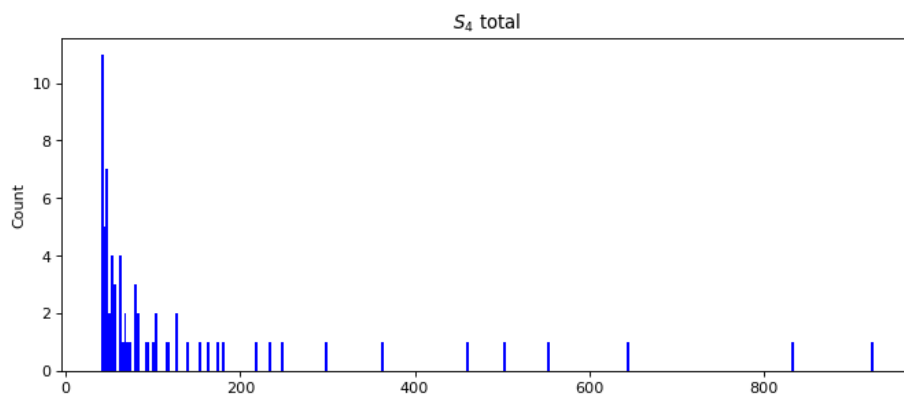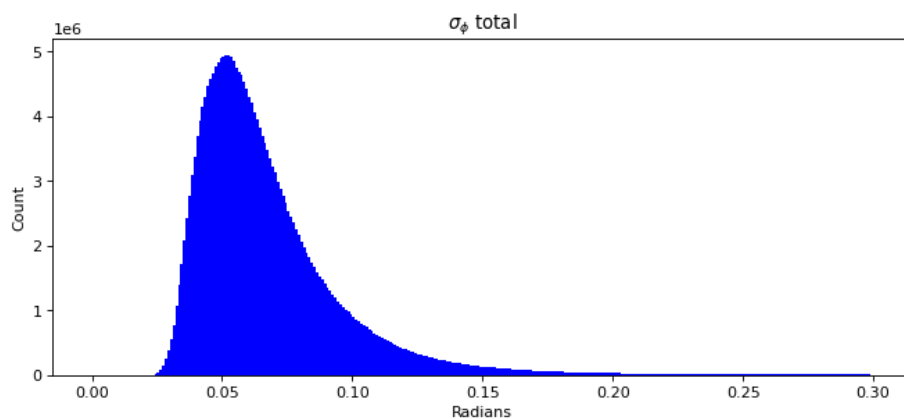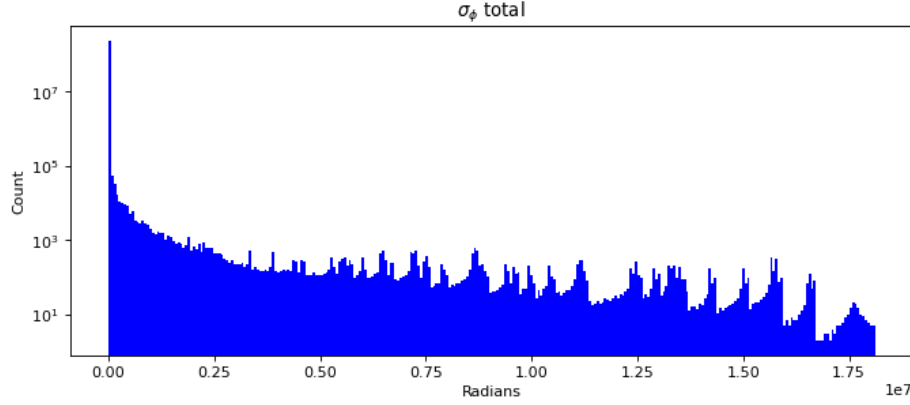scintillations had found that the line of sight azimuth and elevation angle of the satellite has a peak variation in the power and phase values at 90° and 73°, respectively [Deshpande et al., 2014], [Deshpande]. The elevation angle of 73° was aligned vertically with Earth's magnetic field in the simulation and the study showed that greatest scintillation occurs when irregularities are elongated along the propagation direct, as is the case with field-aligned irregularities. In light of this, we've plotted some CERTO events with the highest elevation to observe and see how true this is for our data.

There were also very few cases where the data did not produce large fluctuations with high elevation leading to perceived strong scintillation in otherwise quiet regions. Two such examples are shown in Figure 3.14.

3.3.2 Average Total σ_ϕ Scintillation as a Function of Elevation Angle

In this section we present data of σ_ϕ scintillations as a function of elevation to learn whether the increasing elevation angle in correlation with as increasing σ_ϕ value theorized in Section 3.3.1 is significant. The data in this section is gathered from the total set of CERTO data gathered from 2017-2018. The binning used for this data equates 1 bin per 5° of elevation angle and 18° of azimuth angle.
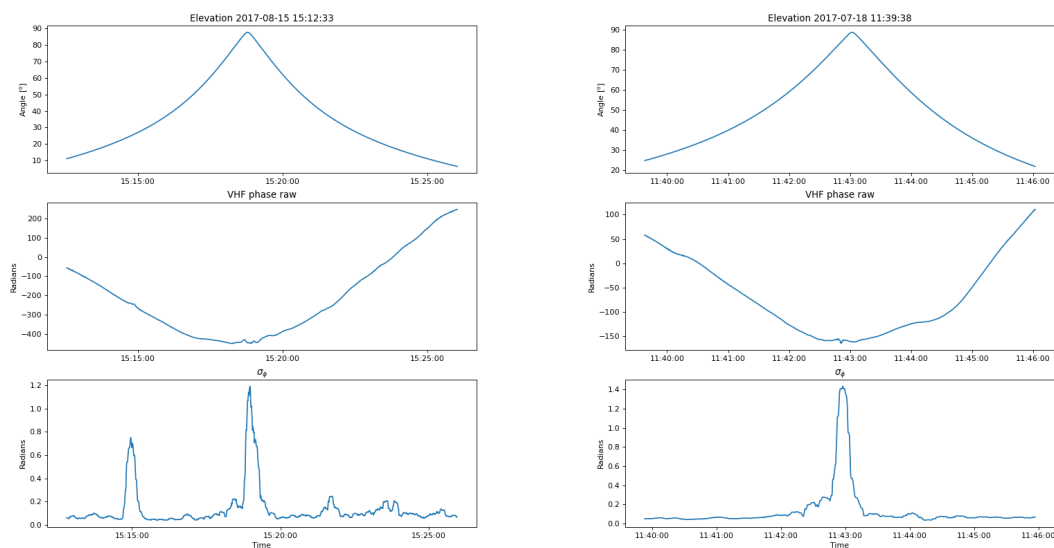
(a) Plots from top to bottom: elevation, raw VHF phase, σ_ϕ

(b) Plots from top to bottom: elevation, raw VHF phase, σ_ϕ

Figure 3.12: Example VHF σ_ϕ plots with scintillation peaks during peak elevation.
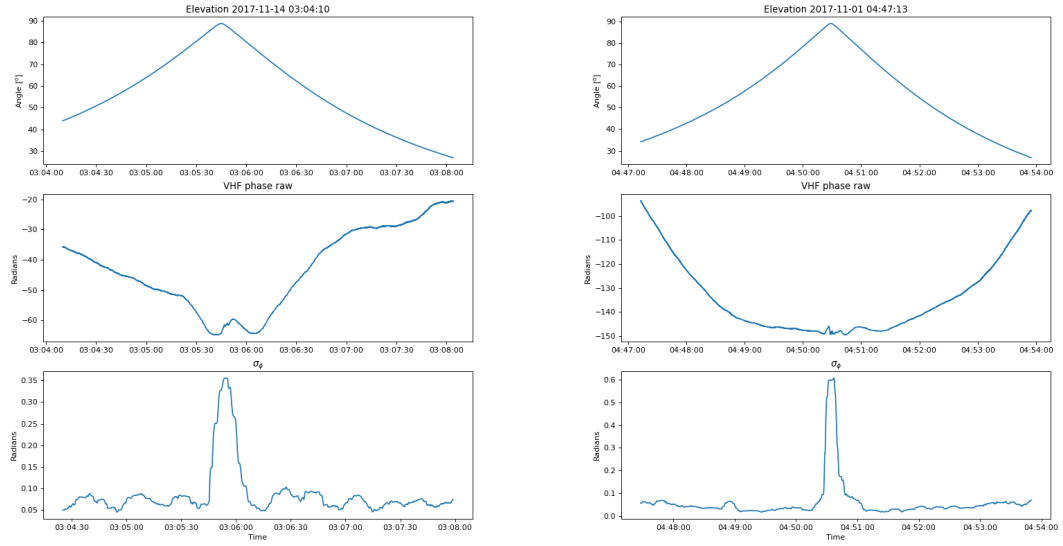
(a) Plots from top to bottom: elevation, raw VHF phase, σ_ϕ

(b) Plots from top to bottom: elevation, raw VHF phase, σ_ϕ

Figure 3.13: Example VHF σ_ϕ plots with scintillation peaks during peak elevation with otherwise quiet data.
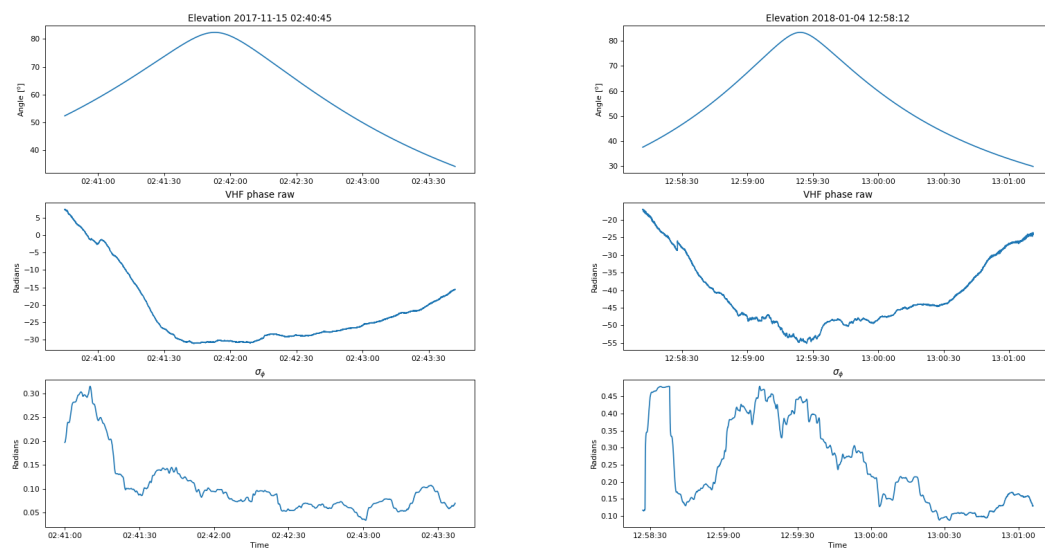
(a) Plots from top to bottom: elevation, raw VHF phase, σ_ϕ

(b) Plots from top to bottom: elevation, raw VHF phase, σ_ϕ

Figure 3.14: Example VHF σ_ϕ plot without scintillation peaks during peak elevation.

Figure 3.15 shows a plot of σ_ϕ averaged over the satellites elevation angle to Resolute Bay at the time of recording the data. This plot shows a positive correlation between elevation angle and σ_ϕ. Some speculation for the occurrence of this phenomena could be that the irregularities in the ionosphere are random except for one direction where they are tube shaped irregularities. As the elevation angle increases this tube shape could become more apparent. Perhaps the irregularities are more coherent when viewed along the vertical axis because they are field-aligned.
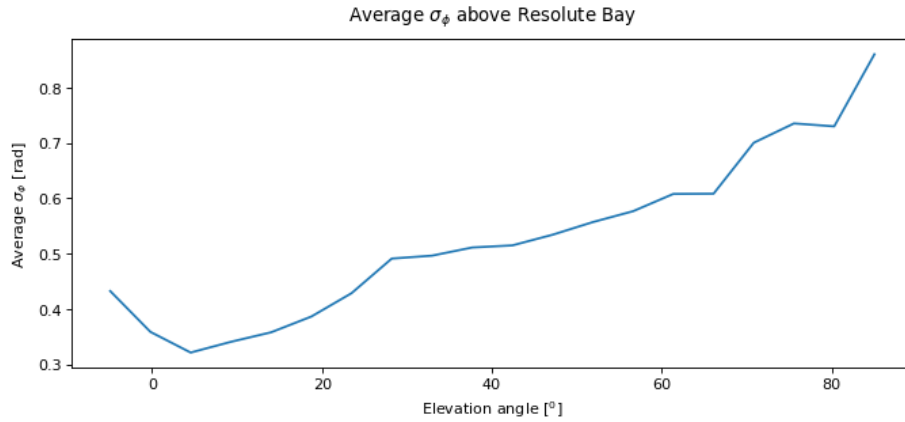
Figure 3.15: A plot of the VHF σ_ϕ averages as a function of elevation.

Figure 3.16 shows the same data as Figure 3.15, but with the standard deviation in each bin added as bars to show the variance in σ_ϕ within the binning of the elevation angle. The standard deviation bars are large because in any givin bin σ_ϕ could be very close to zero if there is no activity or extremely large if there is a large amount of plasma structuring.

Figure 3.17 is a polar plot of the average σ_ϕ with respect to elevation and azimuth angle. The elevation is plotted as the cosine of the elevation angle. The azimuthal angle at $0°$ points towards the geographic north. Within this plot we can see the gradual increasing of average σ_ϕ as elevation angle increases with some notable anomaly near the northern low elevation region that can be explained by observing the data set in its entirety as seen in Figure 3.18. The most notable aspect of this plot is the apparent dependence on azimuth angle and σ_ϕ. The authors do not have any speculation as to why we can see increasing σ_ϕ values in azimuthal angles to the East
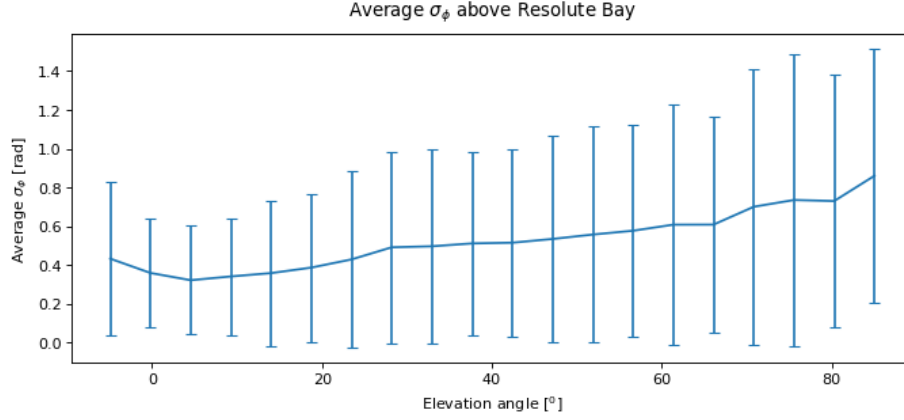
Figure 3.16: A plot of the VHF σ_ϕ averages as a function of elevation with standard deviation bars.

and West.

To better understand the satellite paths responsible for Figure 3.17, we thought to recreate the plot with a bin size so large it would effectively show every satellite path. The resulting plot of this is seen in Figure 3.18. As we can see in this plot, satellites do not often pass by directly North from the horizon above resolute bay. The small amount that did pass by this region also may have coincidentally have had larger σ_ϕ values which may lead us to believe this region has more scintillations than it really has. This plot also shows us that most satellite passes occur to the Northern North East and the Northern North West. There are also considerably less passes that reach elevation angles overhead (80°-90°) than there are passes elsewhere.

3.3.3 Case Studies of the Highest σ_ϕ Scintillation Events

In this section we will display and discuss the individual events responsible for all VHF $\sigma_\phi > 6$ rad. The extreme examples of scintillation that we see in this section do not have known sources owing to lack of contextual data allowing us to identify these. However, one might speculate that these are due to hot or cold polar cap patches or potentially polar auroral precipitation [Zhang et al., 2017], [Zhu et al., 1997]. Most of these events seem to be due to a discrete feature in the phase, rather than a period of sever fluctuation. Some may not call these strictly "scintillation" events, but they

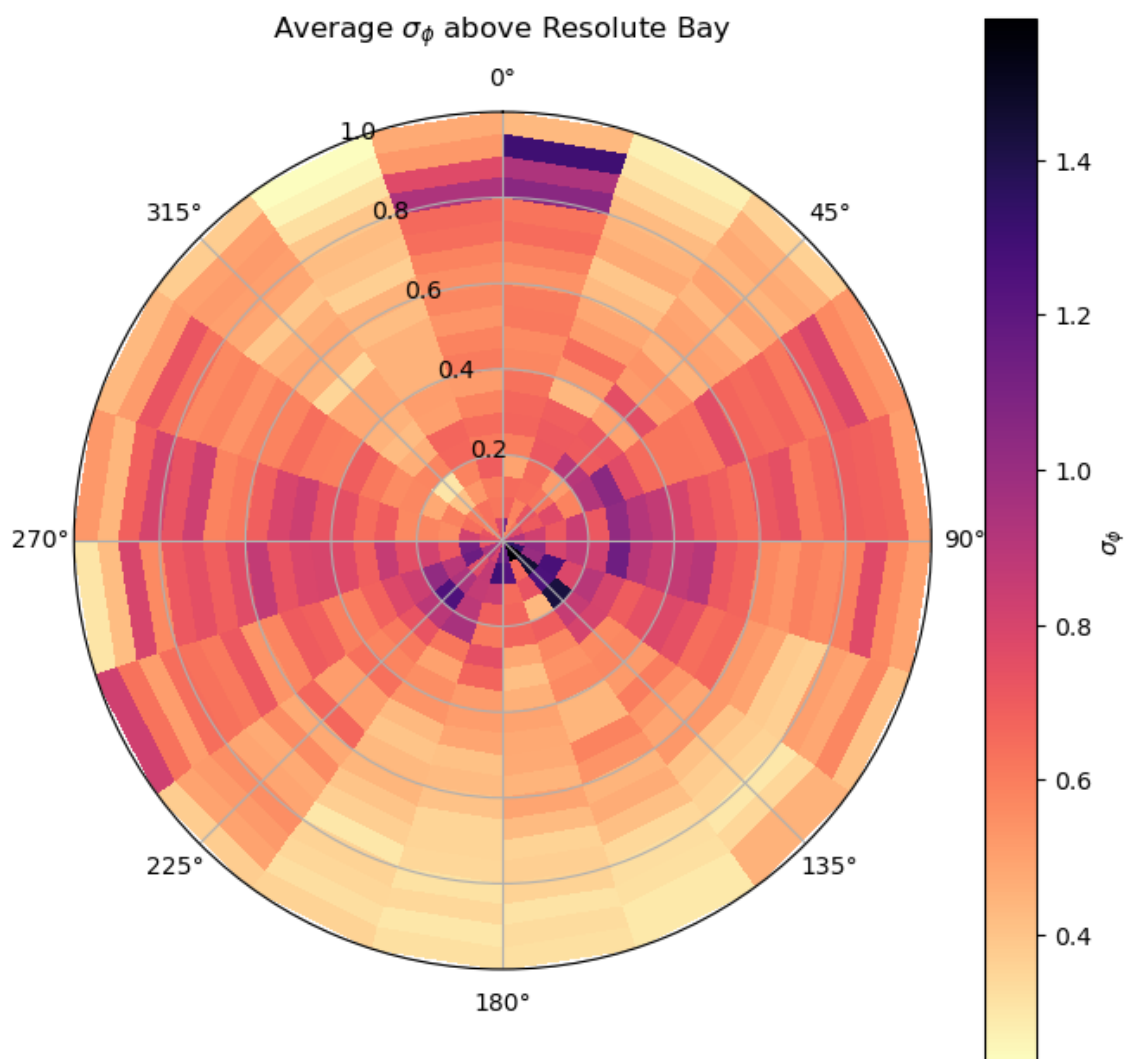Figure 3.17: A plot of the VHF σ_ϕ averages as a function of elevation and azimuth angle. Here the elevation is plotted as the cosine of the elevation angle.
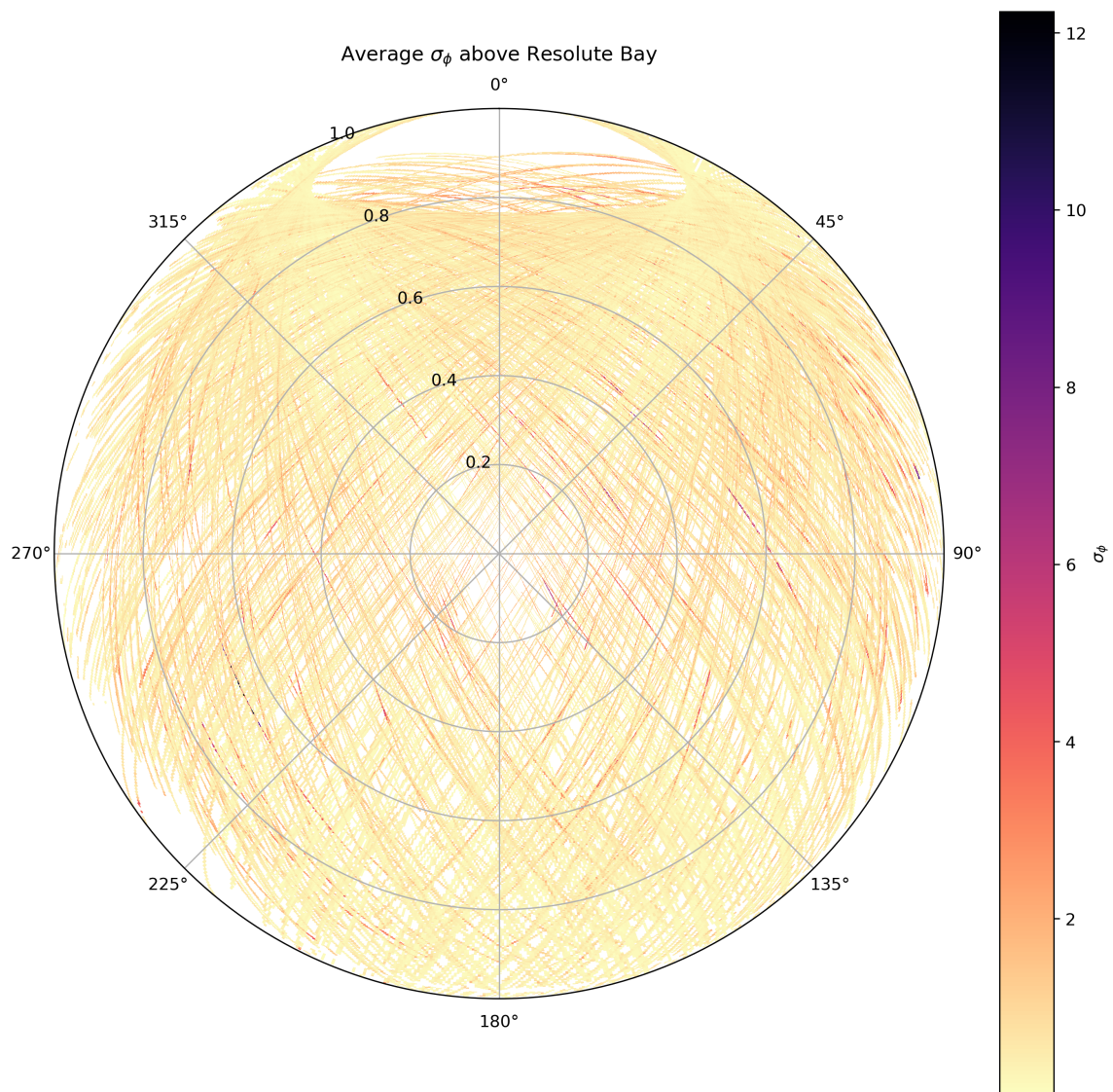
Figure 3.18: A plot of the VHF σ_ϕ with many bins to illustrate satellite paths over Resolute Bay and provide perspective to the distribution of data. Here the elevation is plotted as the cosine of the elevation angle.

are important to discuss. We will attempt to measure the scale size of the structuring within the ionosphere by observing the duration of the identified cause of scintillation within the raw phase data and multiply it by an estimated speed of the satellite orbit at the IPP height. LEO satellites move at about 8 km/s and since the IPP is at roughly half of the satellites altitude the speed at the IPP should be about 4 km/s. Table 3.1 summarizes the results of the scale sizes and is shown at the end of this section.

We will begin with the more suspect plots displayed in Figures 3.19 & 3.20a. We find these plots to be suspicious because they occur at the ends of the event, the plots in Figure 3.19 in particular are strange as even if we took the data at face value, a plot at these ends has such a low elevation angle to Resolute Bay it would be difficult to determine the true scale or existence of the structuring within the ionosphere. Another problematic point of interest can be seen in Figure 3.19a with the "jump" in the raw phase data at about 12:54:45. This rapid fluctuation is likely what is causing the calculated σ_ϕ to peak. The raw phase data in Figure 3.19b features no such sharp jumps and the only visible part of the data responsible for the peak in the resulting calculated σ_ϕ plot is either the sharp incline a little bit before 15:56:30 or the small dip followed by a less sharp incline starting at 15:56:30.

Figure 3.20a is challenging to analyze for different reasons to the previous two plots. The peak does start at the beginning unlike the end for the last two, but this isn't the main concern. When the raw data gets flagged, as mentioned in Section 2.1, it splits the data into two time series. In the case of this plot, a flag existed during the peak elevation angle as evident by the elevation plot starting at 90°. The cut out part of this whole event from the left side likely has noticeable scintillation as the data also cutoffs at 90° at the end. Because of this discontinuity we think that the scintillation could be a different value had the data remained continuous without large fluctuations in the flagged region. Along with this, the scale size of the structuring is also difficult to identify. In short, there is likely strong scintillation and present in this range, but the true value of the scintillation may be different than what was calculated in the plot because of the discontinuous data. Figure 3.20b shows the only scintillation event during the mid section of the data where a peak occurs away from
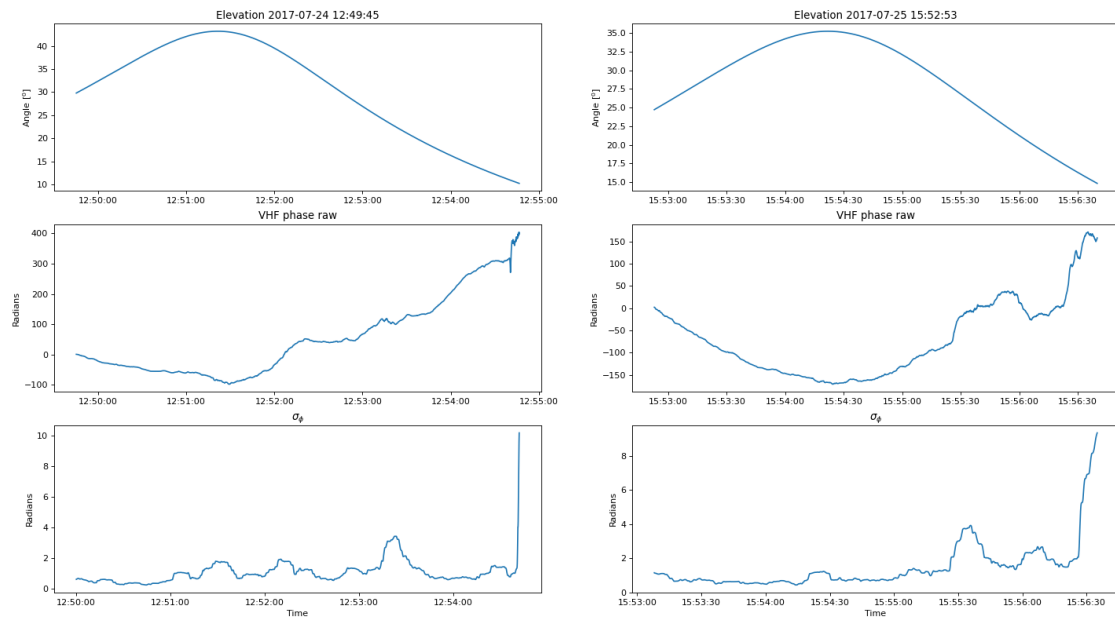
(a) Plots from top to bottom: elevation, raw VHF phase, σ_ϕ

(b) Plots from top to bottom: elevation, raw VHF phase, σ_ϕ

Figure 3.19: Plots with suspect VHF σ_ϕ data peaking at the end.

the peak elevation. The scintillation is likely caused by the sharp incline at about 14:44:50. If we were to estimate the scale size of the structure here in spite of the low elevation angle while the peak itself is off center from the peak elevation angle, we would estimate it to be about 4 km.
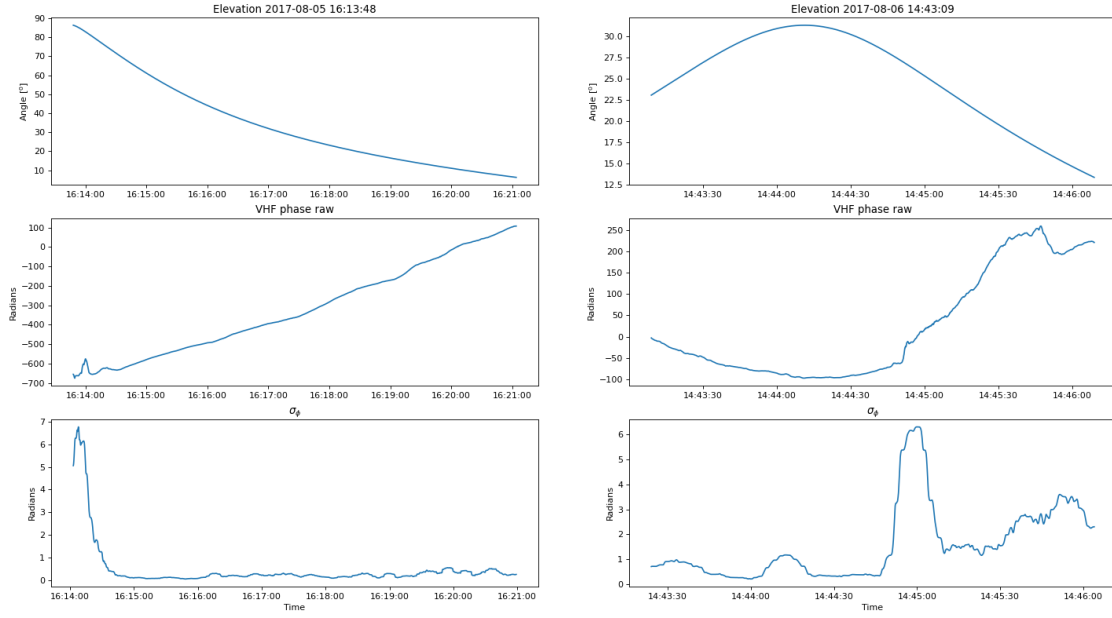
(a) Plots from top to bottom: elevation, raw VHF phase, σ_ϕ

(b) Plots from top to bottom: elevation, raw VHF phase, σ_ϕ

Figure 3.20: A plot of suspect VHF σ_ϕ data peaking at the beginning (left) and a plot of the only high scintillation data in this section that has the main peak located away from the peak elevation (right).

Interestingly, Figure 3.20a was flagged near it's peak elevation angle during a measurement of a supposed scintillation causing structure. If we go into the data and pick out the time series before this flag and place them side by side in Figure 3.21 we can see that the scintillation event was interrupted by a flag within the data. Had this region not been flagged and these two time splits were combined we would likely see a continuous plot that showed strong scintillation. This plot leads us to speculate that perhaps this particular scintillation event was strong enough to set the flag mechanism off as a false positive.

Figures 3.22 & 3.23 show four plots where there is one singular peak in σ_ϕ that
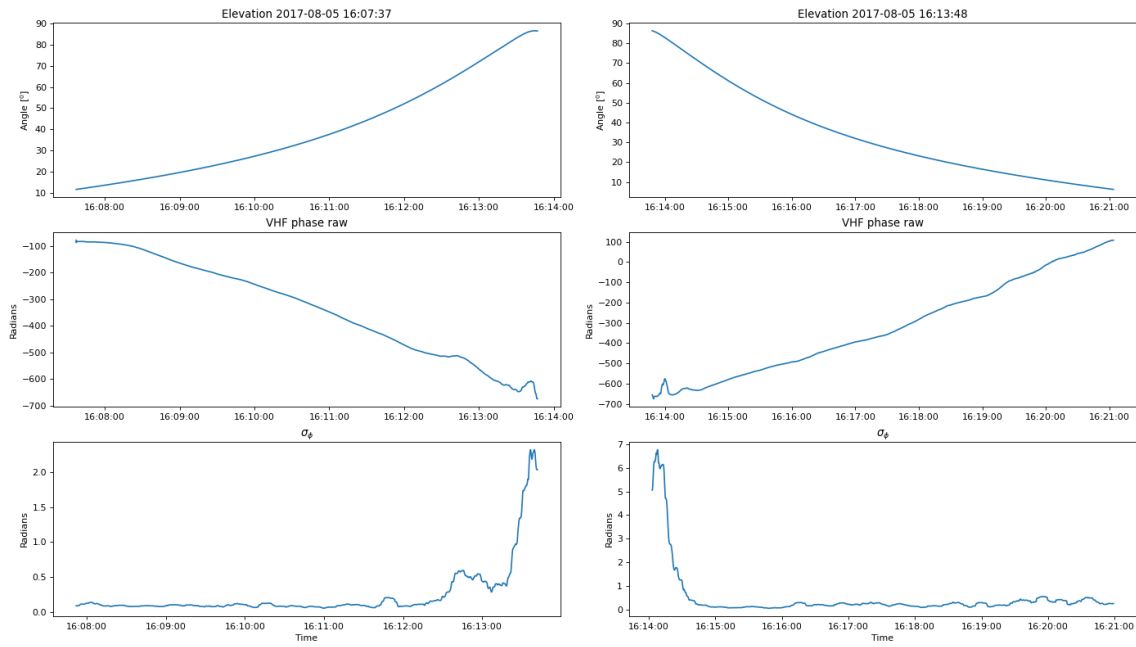
Figure 3.21: A plot of VHF σ_ϕ cut in half during a scintillation event. The right plot is the same as Figure 3.20a.

can be identified in the raw phase plot. Other than these peaks, the data is also
mostly quiet and there isn't much else to discuss about these plots other than scale
size of the structure that they imply. Figure 3.22a has a scintillation event stemming
from the phase perturbations in the raw data from about 14:41:55 to 14:42:15, so the
estimated scale size should be 80 km with both of the "humps" in the data with a
scale size of about 40 km each. Figure 3.22b has a scintillation event stemming from
the single mound in the raw data starting from about 13:31:30 and lasting about 67.5
seconds, so the estimated scale size should be about 270 km.

(a) Plots from top to bottom: elevation, raw
VHF phase, σ_ϕ

(b) Plots from top to bottom: elevation, raw
VHF phase, σ_ϕ
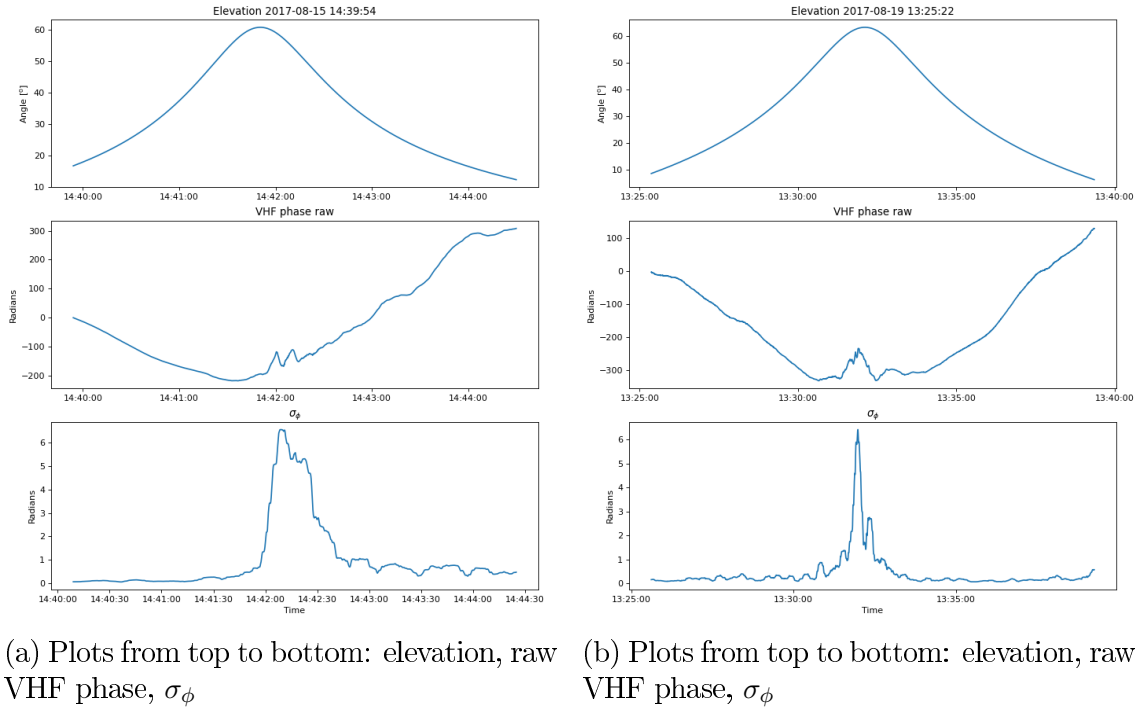
Figure 3.22: Plots of VHF σ_ϕ with singular notable peaks in the data

Figure 3.23a has a scintillation event stemming from the sudden phase decrease
in the raw data starting from about a minute or so behind 14:00:00 and lasting about
18 seconds, so the estimated scale size should be about 72 km. Interestingly, this
plot features what is likely a plasma depletion instead of an enhancement that the
other plots show. Figure 3.23b is the least quiet of this group of four plots and so
measuring the scale size is more complicated. Instead two scale sizes are computed,

one for the singular large peak visible in the raw phase data from about 11:20:32 to 11:20:40 as 32 km, and one for the larger structure responsible for $\sigma_\phi > 1$ starting from about 11:20:20 to 11:21:00 in the raw phase data to have a scale size of 160 km.

(a) Plots from top to bottom: elevation, raw VHF phase, σ_ϕ

(b) Plots from top to bottom: elevation, raw VHF phase, σ_ϕ
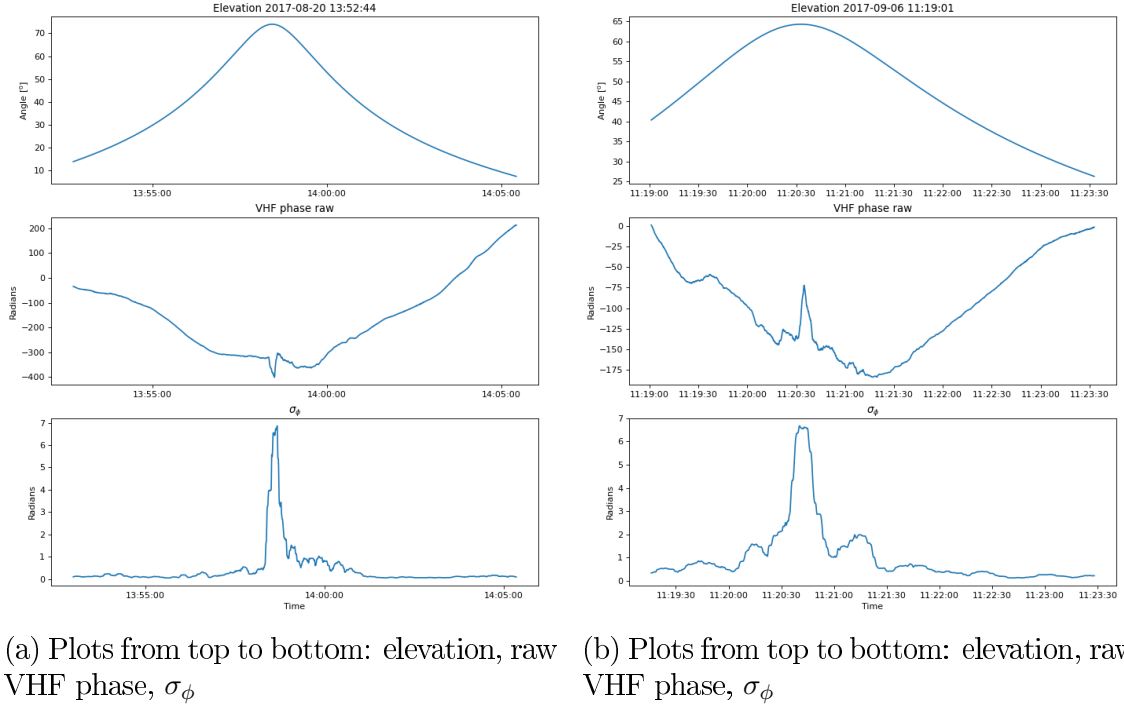
Figure 3.23: Plots of VHF σ_ϕ with singular notable peaks in the data (cont.)

Figure 3.24 shows two plots where the calculated σ_ϕ is mostly always above 1 rad. As each of these events are likely structures of varying size overlapping each other we only find it reasonable to measure the scale size of what is responsible for the largest peaks in the raw phase data. Figure 3.24a has the strongest scintillation event stemming from the small mound in the raw data from about 16:06:00 to 16:06:10, so the estimated scale size should be 40 km. Figure 3.24b has the strongest scintillation event stemming from the the raw data from about 22:41:45 to 22:42:0, so the estimated scale size should be 60 km.

Figure 3.25 shows the highest VHF σ_ϕ scintillation values obtained from CERTO. Looking at this plot compared to the more suspect plots in Figures 3.19 & 3.20 we can see that there are no similar signs of dubious looking raw phase data that we
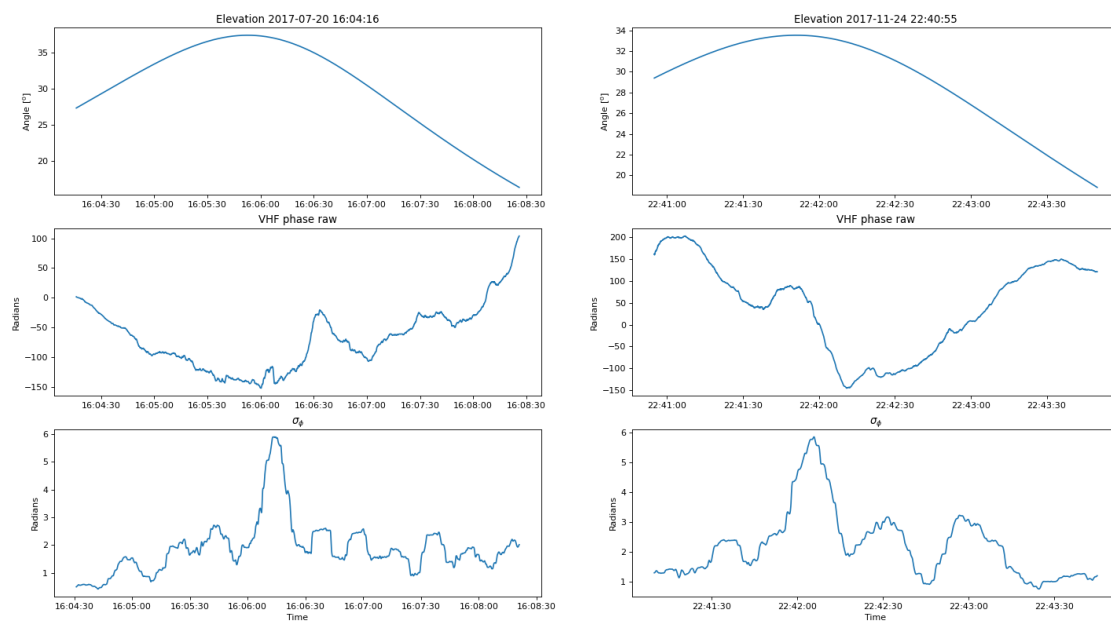
(a) Plots from top to bottom: elevation, raw VHF phase, σ_ϕ

(b) Plots from top to bottom: elevation, raw VHF phase, σ_ϕ

Figure 3.24: Plots of VHF σ_ϕ with mostly high scintillation occurences, $\sigma_\phi > 1$

might have expected, had we just seen the small amount of points at the end of
the histogram in Figure 3.7. This event also happens to provide two very clear and
separate structures. The larger point of the two, starting a little before 17:35:30
and lasting about 4 seconds gives an estimated scale size of 16 km. The second,
smaller point, occurs around 17:35:50 and has a duration of about 3 seconds, giving
an estimated scale size of 12 km.
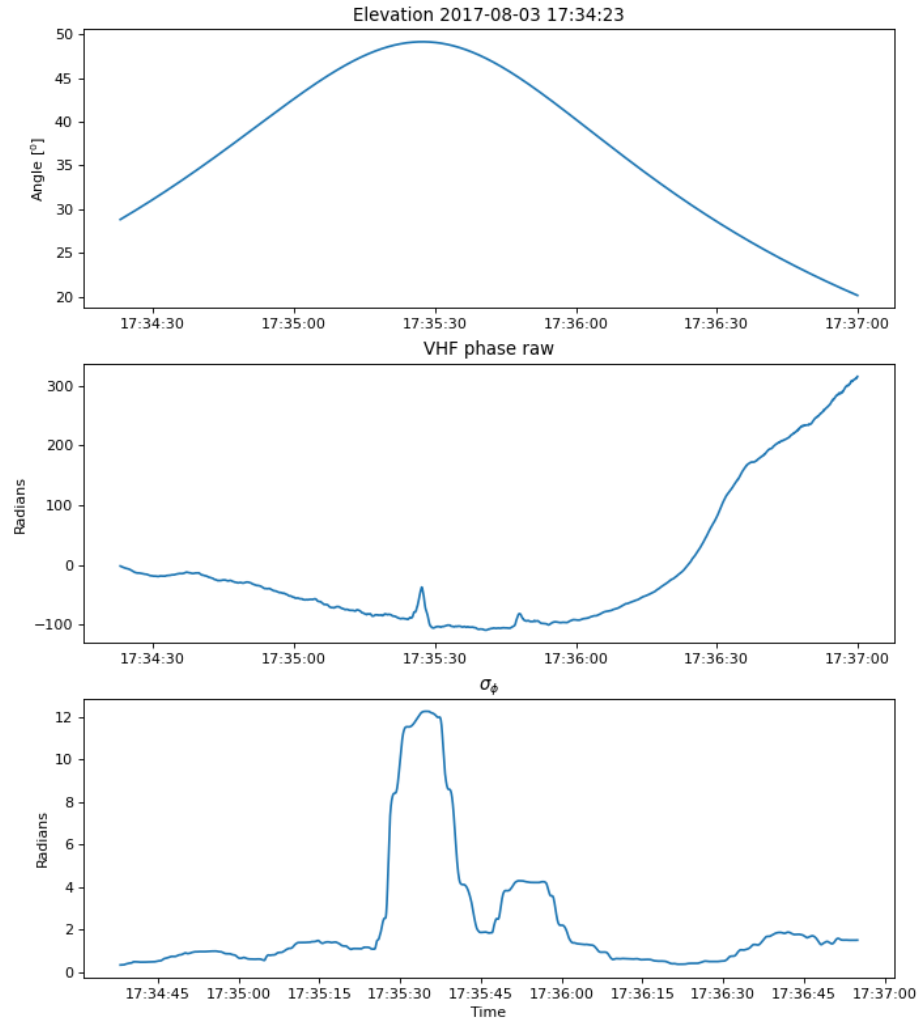
Figure 3.25: A plot of the VHF σ_ϕ event responsible for the peak in the tail end of
the VHF histogram shown in 3.7.

Table 3.1: Table showing the scale sizes of the structures responsible for the high scintillation indices.

Figure	Scale size
3.19a	None
3.19b	None
3.20a	Unknown
3.20b	4 km
3.22a	80 km
3.22b	270 km
3.23a	32 km
3.23b	160 km
3.24a	40 km
3.24b	60 km
3.25a	16 km
3.25b	12 km

Chapter 4

CONCLUSIONS

4.1 Summary

In this thesis, multifrequency scintillation data gathered from two receivers in the polar cap, CERTO and CHAIN. CERTO is a constellation of radio beacons that take measurements of ionospheric TEC and radio scintillations at VHF and UHF. CHAIN is a distributed array of radio instruments primarily in the polar cap that, for the purposes of this thesis, gather L-band scintillation data. This thesis analyzed data gathered by two of these receivers located at Resolute Bay. These different frequency scintillation data were collected and analyzed in an attempt to garner more understanding of how scintillation and scintillation processing differ at varying frequencies.

Chapter 2 detailed the methodology of gathering and processing scintillation data, in particular, Section 2.1 details the complexity and challenge of processing the VHF phase data from CERTO when compared to the processing of the L-band scintillation data from CHAIN in Section 2.2. Section 2.3 detailed the process of the satellite conjunctions that were created to view CERTO and CHAIN events that occurred simultaneously and with an IPP in close proximity to each other. Chapter 3 illustrates the results of this thesis pertaining to satellite conjunctions, histograms of the entire data set, and insight into VHF σ_ϕ from CERTO.

4.2 Conclusions

The key takeaway from this thesis is that scintillation data at wavelengths other than L-band posses different behavior and must be processed meticulously. This factor is compounded by the fact that satellite orbits measuring VHF data travel at LEO and are much faster which results in shorter passes. Within Section **??** we note that for the given satellite conjunction the trend of σ_ϕ is similar in shape between the VHF and L-band though no significant conclusions have been made regarding this. The histograms presented in Section 3.2, Figures 3.6, 3.8, & 3.10 show that VHF σ_ϕ data covers a larger average set of values than L-band σ_ϕ and S_4 values. Section 3.3.2 demonstrates a result from an earlier study of positive correlation between elevation angle and σ_ϕ shown in Figure 3.17.

4.3 Improvements

The CERTO S_4 data was a complex problem to tackle, similarly to the lengthy process covered for processing the CERTO σ_ϕ data. While this thesis was originally meant to cover both, the σ_ϕ data proved to be a challenging enough subject and we decided to leave analyzing VHF S_4 to the future. Repeating this study with a larger dataset is an aspirational goal for the future. Gathering data at the same location would be ideal, however, the receiver unexpectedly went dark in January 2018 and attempts to fix it have been unsuccessful. Looking directly into the CERTO data processing, we can see that after a window is removed from the beginning during detrending and a half window is removed during the σ_ϕ calculation, 15 seconds of data should be remove, which is what happens. However, the same amount of data should also be removed from the end of the data and yet it seems that less than 15 seconds of data is removed from the end and we believe this shouldn't be the case. We will need to look into this. Figures 3.9 & 3.11 display scintillation index values much higher than what is expected at the L-band and learning why these histograms display these results would involve looking into the individual events responsible for these high values. An improvement on the histograms section in general would involve

how they are created. Currently, when creating the histograms for all total data, the CERTO data removes sections of flagged data before calculating σ_ϕ while the CHAIN data calculates without cropping the flagged CERTO region. This should be fixed by removing CHAIN data where there are regions of flagged CERTO data. Within the current method of exception handling in the code, if a beginning time split of an event is too small after the detrending and scintillation calculation then it will be thrown out as expected, you can't have a data set with no data. However, the exception handling also throws out any sequential time splits for the event. This error should be fixed. Figure 3.17 shows an interesting dependence on azimuth angle on σ_ϕ which is topic of discussion for the future.

Bibliography

Paul A Bernhardt and Carl L Siefring. New satellite-based systems for ionospheric tomography and scintillation region imaging. *Radio science*, 41(05):1–14, 2006.

K. Deshpande, M. Zettergren, A. Spicher, L. Lamarche, M. Hirsch, and M. Redden. Modeling high-latitude F-region ionospheric fluid instabilities: Linear and nonlinear evolution and observational signatures. In Y. Deng, O. Verkhoglyadova, S. Zhang, and T. Nishimura, editors, *Cross-Scale Coupling and Energy Transfer in the Magnetosphere-Ionosphere-Thermosphere System*, chapter 3.2, pages 127–175. Elsevier, Amsterdam, The Netherlands, 2021.

KB Deshpande, GS Bust, CR Clauer, CL Rino, and CS Carrano. Satellite-beacon ionospheric-scintillation global model of the upper atmosphere (sigma) i: High-latitude sensitivity study of the model parameters. *Journal of Geophysical Research: Space Physics*, 119(5):4026–4043, 2014.

Kshitija Deshpande. personal communication.

Biagio Forte and Sandro M Radicella. Problems in data treatment for ionospheric scintillation measurements. *Radio Science*, 37(6):1–5, 2002.

Biagio Forte and Sandro M Radicella. Geometrical control of scintillation indices: What happens for gps satellites. *Radio Science*, 39(5):1–13, 2004.

Hossein Ghobadi, Luca Spogli, Lucilla Alfonsi, Claudio Cesaroni, Antonio Cicone, Nicola Linty, Vincenzo Romano, and Massimo Cafaro. Disentangling ionospheric refraction and diffraction effects in gnss raw phase through fast iterative filtering technique. *GPS Solutions*, 24(3):1–13, 2020.

PT Jayachandran, RB Langley, JW MacDougall, SC Mushini, D Pokhotelov, AM Hamza, IR Mann, DK Milling, ZC Kale, R Chadwick, et al. Canadian high arctic ionospheric network (chain). *Radio Science*, 44(01):1–10, 2009.

Yaqi Jin, Jøran I Moen, and Wojciech J Miloch. Gps scintillation effects associated with polar cap patches and substorm auroral activity: Direct comparison. *Journal of Space Weather and Space Climate*, 4:A23, 2014.

Michael C Kelley. *The Earth's ionosphere: Plasma physics and electrodynamics.* Academic press, 2009.

P M Kintner, B M Ledvina, and ER De Paula. Gps and ionospheric scintillations. *Space weather*, 5(9), 2007.

Margaret Galland Kivelson and Thomas Christopher Russell. *Introduction to space physics.* Cambridge university press, 1995.

Leslie Lamarche. *Plasma Irregularity Production in the Polar Cap F-Region Ionosphere.* University of Alaska Fairbanks, 2017.

Leslie J Lamarche, Roger H Varney, and Carl L Siefring. Analysis of plasma irregularities on a range of scintillation-scales using the resolute bay incoherent scatter radars. *Journal of Geophysical Research: Space Physics*, 125(3):e2019JA027112, 2020.

Sajan C Mushini, PT Jayachandran, RB Langley, JW MacDougall, and D Pokhotelov. Improved amplitude-and phase-scintillation indices derived from wavelet detrended high-latitude gps data. *GPS solutions*, 16(3):363–373, 2012.

Yukitoshi Nishimura, Olga Verkhoglyadova, Yue Deng, and Shun-Rong Zhang. *Cross-scale Coupling and Energy Transfer in the Magnetosphere-ionosphere-thermosphere System.* Elsevier, 2021.

Lijing Pan and Ping Yin. Analysis of polar ionospheric scintillation characteristics based on gps data. In *China Satellite Navigation Conference (CSNC) 2014 Proceedings: Volume I*, pages 11–18. Springer, 2014.

Carl Siefring. Resolute bay certo dataset. personal communication, 2018. Naval Research Laboratory.

Carl L Siefring, Paul A Bernhardt, H Gordon James, and Richard Todd Parris. The certo beacon on cassiope/e-pop and experiments using high-power hf ionospheric heaters. *Space Science Reviews*, 189(1):107–122, 2015.

Roland T Tsunoda. High-latitude f region irregularities: A review and synthesis. *Reviews of Geophysics*, 26(4):719–760, 1988.

Todd Valentic, John Buonocore, Michael Cousins, Craig Heinselman, John Jorgensen, John Kelly, Moyra Malone, Michael Nicolls, and Anthony Van Eyken. Amisr the advanced modular incoherent scatter radar. In *2013 IEEE International Symposium on Phased Array Systems and Technology*, pages 659–663. IEEE, 2013.

AJ Van Dierendonck and B Arbesser-Rastburg. Measuring ionospheric scintillation in the equatorial region over africa, including measurements from sbas geostationary satellite signals. In *Proceedings of the 17th International Technical Meeting of the Satellite Division of The Institute of Navigation (ION GNSS 2004)*, pages 316–324, 2004.

Y Wang, Q-H Zhang, Periyadan T Jayachandran, Mike Lockwood, S-R Zhang, Joran Moen, Z-Y Xing, Y-Z Ma, and Mark Lester. A comparison between large-scale irregularities and scintillations in the polar ionosphere. *Geophysical Research Letters*, 43(10):4790–4798, 2016.

Kung Chie Yeh and Chao-Han Liu. Radio wave scintillations in the ionosphere. *Proceedings of the IEEE*, 70(4):324–360, 1982.

Q-H Zhang, Y-Z Ma, PT Jayachandran, J Moen, Mike Lockwood, Y-L Zhang, JC Foster, S-R Zhang, Y Wang, David R Themens, et al. Polar cap hot patches: Enhanced density structures different from the classical patches in the ionosphere. *Geophysical Research Letters*, 44(16):8159–8167, 2017.

L Zhu, RW Schunk, and Jan Josef Sojka. Polar cap arcs: A review. *Journal of Atmospheric and Solar-Terrestrial Physics*, 59(10):1087–1126, 1997.

Appendix A

RISR data

Electron density at 2017-07-17 17:36:06

Electron density at 2017-07-18 20:00:52

Electron density at 2017-09-30 23:11:37

Electron density at 2017-10-20 02:31:38

Electron density at 2017-10-21 21:08:20

Electron density at 2017-10-23 00:00:51

Electron density at 2017-10-03 01:07:59

Electron density at 2017-10-03 22:00:48